

A pairwise hydrodynamic theory for flow-induced particle transport in shear and pressure-driven flows

Rodrigo B. Reboucas¹, Alexander Z. Zinchenko² and Michael Loewenberg¹,†

(Received 3 November 2021; revised 2 July 2022; accepted 13 August 2022)

An exact pairwise hydrodynamic theory is developed for the flow-induced spatial distribution of particles in dilute polydisperse suspensions undergoing two-dimensional unidirectional flows, including shear and planar Poiseuille flows. Coupled diffusive fluxes and a drift velocity are extracted from a Boltzmann-like master equation. A boundary layer is predicted in regions where the shear rate vanishes with thickness set by the radii of the upstream collision cross-sections for pair interactions. An analysis of this region yields linearly vanishing drift velocities and non-vanishing diffusivities where the shear rate vanishes, thus circumventing the source of the singular particle distribution predicted by the usual models. Outside of the boundary layer, a power-law particle distribution is predicted with exponent equal to minus half the exponent of the local shear rate. Trajectories for particles with symmetry-breaking contact interactions (e.g. rough particles, permeable particles, emulsion drops) are analytically integrated to yield particle displacements given by quadratures of hard-sphere (or spherical drop) mobility functions. Using this analysis, stationary particle distributions are obtained for suspensions in Poiseuille flow. The scale for the particle distribution in monodisperse suspensions is set by the collision cross-section of the particles but its shape is almost universal. Results for polydisperse suspensions show size segregation in the central boundary layer with enrichment of smaller particles. Particle densities at the centreline scale approximately with the inverse square root of particle size. A superposition approximation reliably predicts the exact results over a broad range of parameters. The predictions agree with experiments in suspensions up to approximately 20% volume fraction without fitting parameters.

† Email address for correspondence: michael.loewenberg@yale.edu

© The Author(s), 2022. Published by Cambridge University Press. This is an Open Access article, distributed under the terms of the Creative Commons Attribution licence (http://creativecommons.org/licenses/by/4.0), which permits unrestricted re-use, distribution and reproduction, provided the original article is properly cited.

¹Department of Chemical and Environmental Engineering, Yale University, New Haven, CT 06520-8286, USA

²Department of Chemical and Biological Engineering, University of Colorado, Boulder, CO 80309-0424, USA

Key words: suspensions, coupled diffusion and flow, particle/fluid flows

1. Introduction

Particles in a fluid subjected to a bulk deformation interact with each other hydrodynamically, modifying the rheology of suspensions, and can lead to flow-induced microstructuring (Stickel & Powell 2005; Van der Sman 2009; Denn & Morris 2014; Tanner 2018; Carotenuto *et al.* 2021). Flow-induced microstructure in flowing suspensions is a key to understanding a diverse range of natural phenomena and is fundamental to the engineering design of these systems. Flow-induced microstructure is important in materials processing, such as the production of particle-filled polymers (Migler 2001; Elias *et al.* 2008; Colón Quintana *et al.* 2019), and ceramic tape casting (Jabbari *et al.* 2016). Rheology and microstructure affect the sensation of food and digestion (Lentle & Janssen 2010; Schroen, de Ruiter & Berton-Carabin 2020). Flow-induced demixing in polydisperse suspensions is a useful separation technique (Bandyopadhyay, Peralta-Videa & Gardea-Torresdey 2013; Schroen, van Dinther & Stockmann 2017).

The effects of suspension microstructure are especially pronounced in tightly confined flows as arise in microfluidic devices (Van Dinther *et al.* 2012; Sarkar & Singh 2013; Dahl *et al.* 2015; Singha *et al.* 2019) and hydrofracturing (Barbati *et al.* 2016; Osiptsov 2017). Blood flow in the microcirculation depends critically on the coupled rheology and flow-induced microstructure (Secomb 2017). The Fahraeus–Lindqvist effect refers to the concomitant reduction in haematocrit and viscosity in capillaries and small vessels (i.e. arterioles, venules). In their classical paper, Fahraeaus & Lindqvist (1931) explain these phenomena in terms of the migration of red blood cells (erythrocytes) to the region of faster-moving fluid at the centre of the capillary where velocity gradients are smaller. This mechanism is important for reducing the workload on the heart and helps to understand the detrimental effects of certain diseased states (e.g. malaria, sickle-cell anaemia) that disrupt this mechanism by altering the mechanical properties of red blood cells (Higgins *et al.* 2007; Diez-Silva *et al.* 2010; Chien, Gompper & Fedosov 2021). This phenomenon continues to be an active area of study (Pries, Neuhaus & Gaehtgens 1992; Tokarev, Panasenko & Ataullakhanov 2011; Secomb & Pries 2013).

Investigations of flow-induced structuring have focused on suspensions of spherical particles suspended in Newtonian liquids (Karnis, Goldsmith & Mason 1966; Koh, Hookham & Leal 1994; Hampton et al. 1997; Lyon & Leal 1998a,b). Low-Reynolds-number and large-Péclet-number conditions usually apply, based on the size of the suspended particles, the fluid viscosities and typical shear rates. Under these conditions, fluid motion is governed by the Stokes equations and Brownian motion is negligible (Duprat & Stone 2015). Early studies include experimental measurements (Eckstein, Bailey & Shapiro 1977; Leighton & Acrivos 1987a) and computer simulations (Bossis & Brady 1987; Chang & Powell 1994) of self-diffusion of marked tracer particles in sheared suspensions. Eckstein et al. (1977) proposed a hydrodynamic self-diffusivity, $D_s \sim \dot{\gamma} a^2$, resulting from O(a) random particle displacements with zero mean due to uncorrelated hydrodynamic interactions between particles occurring at a rate of $\dot{\gamma}$, where a is the particle radius, $\dot{\gamma}$ is the magnitude of the shear rate and the proportionality depends on the volume fraction. Leighton & Acrivos (1987b) proposed the existence of a cross-flow particle flux down the particle concentration gradient with a similarly scaled hydrodynamic diffusivity, $D \sim D_s$, and a particle drift velocity, V, from high to low shear stress (Koch 1989). The ratio of the hydrodynamic self- and gradient diffusivities to the molecular diffusivity, \mathcal{D} associated with Brownian motion, defines a Péclet number, $\dot{\gamma}a^2/\mathcal{D}$; under large-Péclet-number conditions, hydrodynamic diffusion dominates Brownian diffusion (Semwogerere, Morris & Weeks 2007).

The Leighton & Acrivos (1987b) theoretical framework was used to explain the anomalous time-varying viscosity previously observed by Gadala-Maria & Acrivos (1980) (Koch 1989) and provides the basis for the diffusive flux model of suspensions (Phillips *et al.* 1992). The diffusive flux model has been subsequently used to describe the flow-induced microstructure and rheology of suspensions and emulsions (King & Leighton 2001; Ramachandran, Loewenberg & Leighton 2010; Reboucas *et al.* 2016). Although based on pairwise particle interactions, the diffusive flux model provides a phenomenological description for the coupled microstructure and rheology in concentrated suspensions through the use of an empirical model for the concentration-dependent shear viscosity (Eilers 1943; Krieger 1972) and transport coefficients determined from experimental data (Phillips *et al.* 1992).

An alternate suspension balance model was developed where particle fluxes result from normal stress differences (Nott & Brady 1994; Morris 2009). The suspension balance model has also been widely used to explore the flow-induced microstructure and rheology of suspensions. The suspension balance and diffusive flux models are similar; moreover, the diffusive flux model can be derived from the suspension balance model (Nott & Brady 1994; Nott, Guazzelli & Pouliquen 2011). Both are phenomenological descriptions.

Both models have difficulty describing particle distributions at points where the local shear rate vanishes, e.g. at the centre of a Poiseuille flow, as anticipated by Leighton & Acrivos (1987b). At these points, the predicted particle concentration profile has an unphysical singularity. The incorporation of a viscosity model in the diffusive flux model that diverges at a prescribed maximum packing fraction of particles prevents the volume fraction from diverging (Phillips et al. 1992). However, this imposes a volume fraction equal to the prescribed maximum packing fraction at points where the shear rate vanishes which is unlikely to apply in dilute systems. The resulting cusp-shaped distribution reflects the lack of a length scale imposed by the particle size in the diffusive flux model. The use of an ad hoc non-local shear rate or a constitutive model relating stresses to velocity fluctuations rather than the local shear rate smooths the cusp that would otherwise be predicted by the suspension balance model (Morris & Brady 1998; Frank et al. 2003). Away from singular points where the shear rate vanishes, the particle concentration profiles predicted by the diffusive flux and stress balance models are in qualitative agreement with experimental measurements (Lyon & Leal 1998a; Frank et al. 2003).

Experiments reveal size segregation in bidisperse suspensions (Husband *et al.* 1994; Lyon & Leal 1998*b*; Semwogerere & Weeks 2008). These studies tend to show that larger particles accumulate more quickly in regions of low shear rate. Slow evolution of the particle microstructure requires long entry lengths to attain fully developed stationary particle distributions (Nott & Brady 1994; Phan-Thien & Fang 1996), and experiments are often later found to have used insufficient entry lengths. Theoretical and phenomenological models are at an early stage. The diffusive flux model has been extended to bidisperse suspensions but requires more adjustable parameters (Shauly, Wachs & Nir 1998; Kanehl & Stark 2015; Chun *et al.* 2019; Reddy & Singh 2019), and it fails at points where the shear rate vanishes, leading to predictions at odds with experiments.

Many-particle boundary integral simulations with periodic boundary conditions have been used to explore particle segregation in wall-bounded shear- and pressure-driven flows of polydisperse suspensions of deformable particles, e.g. red cells and platelets (Zhao & Shaqfeh 2011; Zhao, Shaqfeh & Narsimhan 2012). These studies focused on size segregation that occurs in small channels, several particle diameters wide (e.g. arterioles, venules). The results further a fundamental understanding of the Fahraeus–Lindqvist effect and related phenomena such as plasma skimming (Tangelder *et al.* 1985; Aarts *et al.* 1988), showing that smaller, stiffer particles (platelets, and white cells) accumulate near bounding walls of a channel and larger, more deformable particles (red cells) accumulate in the central, core region of the flow ('anti-margination'). Aside from the restriction to creeping flow conditions, which may not always apply, a drawback of boundary integral simulations is their extreme computational intensity which hinders access to the long-time stationary microstructure of these systems.

Kinetic theory models, based on the Boltzmann equation, provide another useful theoretical framework for suspension flows (Kumar & Graham 2012; Zurita-Gotor, Bławzdziewicz & Wajnryb 2012; Narsimhan, Zhao & Shaqfeh 2013; Kumar, Rivera & Graham 2014; Rivera, Sinha & Graham 2015; Rivera, Zhang & Graham 2016; Qi & Shaqfeh 2017, 2018). Central to the Boltzmann equation is the particle flux generated by uncorrelated pair interactions (collisions) between particles suspended in the continuous-phase fluid. Accordingly, the Boltzmann equation is inherently a pairwise description, and thus restricted to dilute systems; however, it may provide a reasonable approximate description for particle microstructure in suspensions with moderate volume fractions. Comparisons between kinetic theory models and direct three-dimensional boundary integral simulations reveal close agreement in the predicted microstructure for volume fractions up to approximately 20 % (Narsimhan et al. 2013; Qi & Shaqfeh 2017, 2018). Although they require much less computation than many-particle boundary integral simulations, kinetic theory models still require considerable computation, preventing parametric exploration of suspension microstructures. Their computational requirement is dominated by the pre-calculation of an ensemble of pair trajectories needed for evaluating the collision flux in the Boltzmann equation, but once pair trajectories are calculated, kinetic theory models provide comparatively efficient access to the long-time, statistically stationary microstructure.

For small channels, several particle diameters wide, the resulting Boltzmann equation can be numerically solved to obtain the particle distribution. Features such as margination and anti-margination are recovered (Kumar & Graham 2012; Zurita-Gotor *et al.* 2012; Narsimhan *et al.* 2013; Kumar *et al.* 2014; Rivera *et al.* 2015; Qi & Shaqfeh 2017, 2018). For channels that are wide compared with particle size, the collision flux can be expanded to yield a phenomenological particle transport equation similar to the diffusive flux model for dilute suspensions (Rivera *et al.* 2016). Note that kinetic theory models have the same difficulty as the diffusive flux and stress balance models at points of vanishing shear rate, requiring a similar *ad hoc* treatment in the neighbourhood of such points (Rivera *et al.* 2016; Qi & Shaqfeh 2017).

Pairwise hydrodynamic interactions of force- and torque-free spherical particles in shear flow under creeping flow conditions are well understood and analytically tractable (Lin, Lee & Sather 1970; Batchelor & Green 1972a,b; Zinchenko 1978, 1980, 1983). By the linearity of the Stokes equations and by symmetry, pair interactions between spherical particles on open trajectories in shear flow are reversible, yielding zero net cross-flow displacements of the particles; however, there are diverse phenomena that can break the symmetry of pair trajectories in shear flow, leading to non-zero net displacements. It is generally accepted that particle displacements resulting from irreversible pair interactions are the dominant mechanism for particle transport (Leighton & Acrivos 1987a,b; Phillips et al. 1992).

Mechanisms that break the symmetry of pair interactions include the perturbative effects that slightly affect hydrodynamic pair interactions and short-range phenomena that qualitatively affect the motion of particles when they are in near contact with surface-to-surface separations $h_0 \ll a$ but have a negligible effect at larger separations. Short-range phenomena involve symmetry-breaking 'contact' interactions between particles on narrowly offset streamlines of the flow. The classical lubrication singularity between smooth spherical particles hinders the near-contact approach of particles in the compressive quadrant of the shear flow, preventing contact, and acts symmetrically slowing the separation of the particles in the extensional quadrant of the flow. Contact interactions break the symmetry of pair interactions in shear flow because they involve a compressive force that prevents particle overlap in the compressive quadrant of the flow without a compensating tensile force in the extensional quadrant.

The prototypical example of a short-range mechanism for contact interactions is small-amplitude surface roughness, $d \ll a$, that prevents surface-to-surface particle separations less than d (Smart & Leighton 1989; Smart, Beimfohr & Leighton 1993; da Cunha & Hinch 1996; Rampall, Smart & Leighton 1997; Wilson 2005; Ingber & Zinchenko 2012). Other examples of particles with short-range contact interactions include particles with weak permeability (Reboucas & Loewenberg 2021a,b, 2022), particles stabilized by screened electrostatic interactions (Zinchenko 1984; Kremer, Robbins & Grest 1986) and emulsion drops under small-deformation conditions (Loewenberg & Hinch 1997; Ramachandran $et\ al.\ 2010$). Particle-scale deformation associated with stronger flows is an example of a perturbative mechanism, affecting hydrodynamic interactions at O(a) separations, and breaking the symmetry of more distant, non-contacting pair trajectories (Lopez & Graham 2007; Lac & Barthès-Biesel 2008; Singh & Sarkar 2015; Malipeddi & Sarkar 2019a,b).

In this paper, we present a simplified theory for flow-induced structuring in dilute particle suspensions based on pair interactions between particles. In contrast to the phenomenological models discussed above, ours is an exact description. Starting from a Boltzmann-type master equation, particle fluxes are derived for the cross-flow hydrodynamic particle transport in flows such as shear and planar Poiseuille flow. A general analysis is presented for the boundary layer that forms in regions where the shear rate vanishes and for the stationary particle distributions that form away from these regions. Cross-stream displacements for particles that undergo symmetry breaking, contact interactions are formulated in terms of quadratures of mobility functions for spherical particles. Using this result, transport coefficients are explicitly calculated for rough particles and emulsion drops and results are presented for particle distributions in monodisperse and bidisperse suspensions.

The general formulation of the problem, including the Boltzmann equation, is presented in § 2, and expanded to derive transport coefficients including an analysis of the region where shear rates vanish. Generic results for stationary particle distributions are derived in § 3 that are independent of the character of the pair interactions between particles. Trajectories of particles that undergo contact interactions are analytically integrated in § 4 to yield particle displacements formulated as quadratures of standard mobility functions. The results from §§ 3 and 4 are combined in § 5 to obtain spatial distributions of rough particles and emulsion drops in mono- and bidisperse mixtures undergoing planar Poiseuille flow. The predictions are compared with experimental results in the literature. Concluding remarks are made in § 6.

2. Formulation of pairwise theory

2.1. Asumptions and simplifications

The starting point for our simplified theory, presented in § 2.2, is a Boltzmann-type equation for particle transport in a dilute polydisperse suspension of non-Brownian, neutrally buoyant particles undergoing unidirectional flow. Only cross-flow variations of particle concentrations are considered. Wall-induced particle migration is neglected under the assumption that the scale of the flow field is large compared with the particle size. Restricting consideration to stationary particle distributions, the collision fluxes of particle species are set to zero.

The collision flux is expanded for smoothly varying particle distributions in § 2.3 to obtain formulas for transport coefficients describing diffusive and drift fluxes of particle species driven, respectively, by gradients of particle concentrations and shear rate. The formulas are appropriately modified to handle regions with vanishing shear rate, as occurs in pressure-driven flows. The results of this section are combined in § 3 to yield an exact formulation for stationary particle distributions in dilute suspensions.

2.2. Boltzmann equation

We consider particle transport in two-dimensional unidirectional flows,

$$\mathbf{v} = v(X_2)\mathbf{e_1},\tag{2.1}$$

where (X_1, X_2, X_3) describes a Cartesian coordinate system and $e_k(k = 1, 2, 3)$ are the corresponding unit vectors. Velocity field (2.1) includes simple shear and planar Poiseuille flow. The particle distribution evolves in the plane perpendicular to the fluid velocity according to the Boltzmann-type equation

$$\frac{\partial n_i}{\partial t} = -\nabla \cdot F_i,\tag{2.2}$$

where $n_i(X_2, X_3)$ is the number density of type-i particles (i = 1, 2, ..., m). (Explicit time dependence of number density is suppressed here because we investigate stationary particle distributions.) The quantity $F_{ik}(X_2, X_3)(k = 2, 3)$ is the flux of type-i particles in the k-direction resulting from pairwise 'collisions' with other particles,

$$F_{ik}(X_2, X_3) = \sum_{j=1}^{m} F_{ijk}.$$
 (2.3)

Here, F_{ijk} is the contribution to the flux F_{ik} from collisions with type-j particles (j = 1, 2, ..., m) given by the Boltzmann collision integral,

$$F_{ijk} = \int_{-\infty}^{\infty} \int_{-\infty}^{\infty} dx_2^{-\infty} dx_3^{-\infty} \int_{-\Delta X_k^{ij}}^{0} n_i(X_k^{i,-\infty}) n_j(X_k^{j,-\infty}) |v^{ij}| dX_k^{i,-\infty},$$
 (2.4)

where $X_k^{i,-\infty}(k=2,3)$ is the initial distance of particle i from the plane X_k where the flux is evaluated, ΔX_k^{ij} is the displacement of particle i in the k-direction due to its binary encounter with particle j, and

$$x_{k}^{-\infty} = X_{k}^{j,-\infty} - X_{k}^{i,-\infty}, \tag{2.5}$$

is the relative initial position of the particles in the cross-flow plane, i.e. the trajectory offset, as shown in figure 1. Here, $|v^{ij}|$ is the magnitude of the relative velocity between

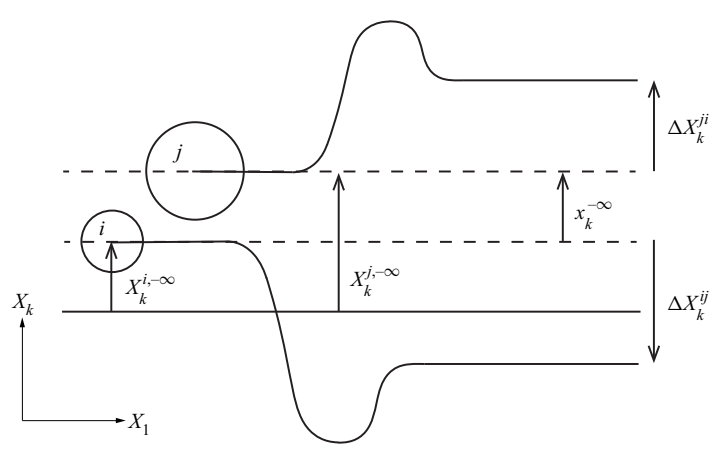


Figure 1. Schematic showing trajectories of particles undergoing pair interaction projected on the 1-k plane (k=2,3); cross-flow displacements ΔX_k^{ij} and ΔX_k^{ji} of particles i and j, respectively; $X_k^{i,-\infty}$ and $X_k^{j,-\infty}$ are coordinates of the particles in cross-flow plane (X_2, X_3) prior to interaction (dashed lines) and $x_k^{-\infty} = X_k^{j, -\infty} - X_k^{j, -\infty}$ $X_{\nu}^{i,-\infty}$ is the initial trajectory offset; particle flux is evaluated at plane of constant X_k (solid line).

widely separated particles,

$$|v^{ij}| = |v(X_2^{j,-\infty}) - v(X_2^{i,-\infty})|, \tag{2.6}$$

and $v(X_2)$ is the prescribed velocity (2.1). Prior to a pair interaction, particles are widely separated in the X_1 -direction (i.e. flow direction) with uncorrelated initial positions $(X_2^{i,-\infty}, X_3^{i,-\infty})$ and $(X_2^{j,-\infty}, X_3^{j,-\infty})$ in the cross-flow plane. Formula (2.4) is obtained using the odd symmetry of particle displacements with respect

to trajectory offset,

$$\Delta X_k^{ij}(-x_k^{-\infty}) = -\Delta X_k^{ij}(x_k^{-\infty}),\tag{2.7}$$

for (k = 2, 3). Particle displacements are, moreover, symmetric with respect to complementary coordinates, i.e.

$$\Delta X_2^{ij}(-x_3^{-\infty}) = \Delta X_2^{ij}(x_3^{-\infty}), \quad \Delta X_3^{ij}(-x_2^{-\infty}) = \Delta X_3^{ij}(x_2^{-\infty}). \tag{2.8a,b}$$

Cross-flow convection due to particle migration away from solid boundaries is omitted from (2.2) under the assumption that flow occurs in a channel that is wide compared with particle size. In the absence of wall interactions that can produce cross-swapping trajectories (Zurita-Gotor et al. 2012; Reddig & Stark 2013), particle displacements obey the relation

$$x_k^{-\infty} \Delta X_k^{ij} \le 0. (2.9)$$

The equality holds only for $x_k^{-\infty} = 0$ and for widely separated particles.

2.2.1. Boundary conditions

Stationary particle distributions are governed by

$$F_i = 0, (2.10)$$

under the assumption that the channel walls are impermeable to the particles. In channel flows, a bulk number density, $n_{i\infty}$, can be imposed for each particle type (i = 1, 2, ..., m),

$$qn_{i\infty} = \int_{S_{\perp}} v(X_2) n_i(X_2, X_3) \, dX_2 \, dX_3, \tag{2.11}$$

where q is the volume flow through a channel with cross-section S_{\perp} .

Diluteness requires low volume fractions,

$$\phi_{i\infty} \ll 1,$$
 (2.12)

where number densities are related to volume fractions, $\phi_i = n_i v_i$, and v_i is particle volume. Stationary particle distributions depend nonlinearly on the bulk composition $n_{i\infty}/n_{\infty}$ given that the particle flux (2.4) is quadratic in number density. However, the total bulk density $n_{\infty} = \sum_{i=1}^{m} n_{i\infty}$ can be scaled out of (2.10) and (2.11). Stationary particle density distributions are proportional to the total bulk number density.

2.3. Particle transport

2.3.1. Local transport coefficients

Here, we analyse particle transport in suspensions undergoing flows with velocity (2.1) and derive diffusive and drift fluxes, i.e. fluxes proportional to the local concentration gradients of particle species and a flux associated with a drift velocity of particles from high to low shear rates. Local transport coefficients for these fluxes are obtained. The diffusive fluxes have been derived previously (Zarraga & Leighton 2001) and a drift velocity has been extracted from a Boltzmann collision integral (Rivera *et al.* 2016). A brief derivation is provided below for completeness and uniformity.

The diffusive and drift fluxes are obtained by evaluating the collision flux (2.4) for perturbative variations in number densities and relative velocities. The number densities and shear rates are expanded up to linear variations

$$n_i = n_{i0} + \sum_{k=2}^{3} \frac{\partial n_i}{\partial X_k} X_k + O(X_k^2),$$
 (2.13)

$$\dot{\gamma} = \dot{\gamma}_0 + \frac{\mathrm{d}\dot{\gamma}}{\mathrm{d}X_2} X_2 + O(X_2^2),\tag{2.14}$$

where $\dot{\gamma}_0$ and n_{i0} , respectively, are the local shear-rate magnitude and number densities of the particles at $X_k = 0$ (k = 2, 3); the quantities $d\dot{\gamma}/dX_2$ and $\partial n_i/\partial X_k$ are the corresponding local values of the derivatives. Brownian motion is neglected under the assumption of large Péclet number

$$\frac{\dot{\gamma}_0 a^2}{\mathcal{D}} \gg 1,\tag{2.15}$$

where \mathcal{D} is the molecular diffusivity. In general, the relative velocity (2.6) becomes

$$|v^{ij}| = |x_2^{-\infty}| \left| \dot{\gamma}_0 + \frac{\mathrm{d}\dot{\gamma}}{\mathrm{d}X_2} \left[X_2^{i,-\infty} + \frac{1}{2} x_2^{-\infty} \right] \right|. \tag{2.16}$$

The development presented in this section assumes a non-vanishing shear rate

$$\dot{\gamma}_0 > \left| \frac{\mathrm{d}\dot{\gamma}}{\mathrm{d}X_2} \right| \left| X_2^{i,-\infty} + \frac{1}{2} x_2^{-\infty} \right|, \tag{2.17}$$

so that the relative velocity (2.16) reduces to

$$|v^{ij}| = |x_2^{-\infty}| \left(\dot{\gamma}_0 + \frac{\mathrm{d}\dot{\gamma}}{\mathrm{d}X_2} \left[X_2^{i,-\infty} + \frac{1}{2} x_2^{-\infty} \right] \right). \tag{2.18}$$

The case of vanishing shear rates is analysed in the next section.

Inserting (2.13) and (2.14) into the flux (2.4) and integrating in $X_k^{i,-\infty}$ yields the net flux of type-*i* particles,

$$F_{ik} = F_{ik}^{(c)} + \delta_{k2} F_{i2}^{(\dot{\gamma})}, \tag{2.19}$$

where $F_{ik}^{(c)}$ are the diffusive fluxes

$$F_{ik}^{(c)} = -D_{ik}^{s} \frac{\mathrm{d}n_{i}}{\mathrm{d}X_{k}} - \sum_{i=1}^{m} \left(D_{ijk} \frac{\mathrm{d}n_{j}}{\mathrm{d}X_{k}} \right), \tag{2.20}$$

and $F_{i2}^{(\dot{\gamma})}$ is the drift flux

$$F_{i2}^{(\dot{\gamma})} = -n_{i0}V_i \frac{\mathrm{d}\dot{\gamma}}{\mathrm{d}X_2}.$$
 (2.21)

The Kronecker delta δ_{pq} in (2.19) indicates that there is a drift flux in the X_2 -direction only.

The above diffusivities and the drift-velocity coefficient are defined by

$$D_{ik}^{s} = \dot{\gamma}_0 \sum_{j=1}^{m} n_{j0} I_{ijk}^{A}, \tag{2.22}$$

$$D_{ijk} = \dot{\gamma}_0 n_{i0} (I_{ijk}^A + I_{ijk}^B), \tag{2.23}$$

$$V_{i} = \sum_{i=1}^{m} n_{j0} \left(I_{ij2}^{A} + \frac{1}{2} I_{ij2}^{B} \right), \tag{2.24}$$

where I_{ijk}^A , I_{ijk}^B are integrals over the relative cross-flow-plane coordinates (2.5)

$$I_{ijk}^{A} = \frac{1}{2} \int_{-\infty}^{\infty} \int_{-\infty}^{\infty} |x_{2}^{-\infty}| (\Delta X_{k}^{ij})^{2} dx_{2}^{-\infty} dx_{3}^{-\infty},$$
 (2.25)

$$I_{ijk}^{B} = -\int_{-\infty}^{\infty} \int_{-\infty}^{\infty} |x_{2}^{-\infty}| x_{k}^{-\infty} \Delta X_{k}^{ij} \, \mathrm{d}x_{2}^{-\infty} \, \mathrm{d}x_{3}^{-\infty}. \tag{2.26}$$

Both integrals are intrinsically positive given the symmetry (2.8a,b) and sign of particle displacements (2.9).

The self-diffusivity of type-i particles, D_{ik}^s , defined by (2.22), can be directly obtained as a sum of the rate of mean squared displacements from random encounters with all particle species. Diffusive fluxes occur in both the velocity gradient and vorticity directions and have contributions from concentration gradients of all species; a non-zero diffusive flux of a species with uniform concentration can be generated by a gradient of another species. This formulation of the diffusive fluxes concurs with that presented by Zarraga & Leighton (2001).

The drift velocities describe the migration of particles from regions of high shear rates. Gradients of the shear-rate magnitude $\dot{\gamma}$ generate an oppositely directed flux. By symmetry, gradients of the shear-rate magnitude do not contribute to the diffusive flux.

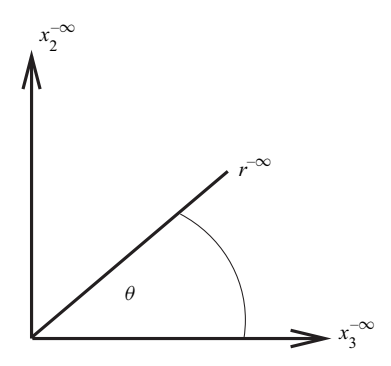


Figure 2. Cylindrical coordinate system $(r^{-\infty},\theta)$ for the cross-flow plane $(x_3^{-\infty},x_2^{-\infty})$, where $x_3^{-\infty}=r^{-\infty}\cos\theta$ and $x_2^{-\infty}=r^{-\infty}\sin\theta$.

The $O(r^{-3})$ far-field velocity gradients of force-free particles perturb the trajectories of deformable particles, where r is distance between the particles normalized by particle size. Integrated along an open trajectory, this perturbation produces pair displacements $\Delta X_k^{ij} = O(r^{-\infty})^{-2}$ for widely offset trajectories, $r^{-\infty} \gg 1$, where $r^{-\infty}$ is the radial relative trajectory coordinate, defined in figure 2. Accordingly, integral (2.26) is divergent. The self-diffusivity of deformable particles can be computed from pair interactions because integral (2.25) converges (Loewenberg & Hinch 1997), but the evaluation of the diffusive and drift fluxes (2.20) and (2.21) requires a numerical cutoff, $r_c^{ij} = r_c^{ji}$, a trajectory offset beyond which interactions between type-i and type-j particles cause cross-flow displacements, i.e.

$$\Delta X_k^{ij} = 0, \quad r^{-\infty} > r_c^{ij}. \tag{2.27a,b}$$

With this cutoff, integrals (2.25) and (2.26) become

$$I_{ijk}^{A} = \frac{1}{2} \int_{0}^{2\pi} \int_{0}^{r_{c}^{ij}} |r^{-\infty} \sin \theta| (\Delta X_{k}^{ij})^{2} r^{-\infty} dr^{-\infty} d\theta, \qquad (2.28)$$

$$I_{ijk}^{B} = -\int_{0}^{2\pi} \int_{0}^{r_{c}^{ij}} |r^{-\infty} \sin \theta| x_{k}^{-\infty} \Delta X_{k}^{ij} r^{-\infty} dr^{-\infty} d\theta, \qquad (2.29)$$

where $(r^{-\infty}, \theta)$ is the cylindrical coordinate system shown in figure 2 and $x_k^{-\infty}$ is defined in the caption.

In general, truncation of the integration domain is an *ad hoc* procedure, and results depend on r_c^{ij} (Narsimhan *et al.* 2013). However, boundary condition (2.27a,b) applies rigorously for spherical particles that undergo contact interactions, as discussed in § 4. Such particles have circular upstream collision cross-sections r_c^{ij} that scale with particle size (Zinchenko 1984; da Cunha & Hinch 1996).

2.3.2. Particle transport at points of vanishing shear rate

Here, the analysis of particle transport developed in the previous section is extended to regions where the shear rate vanishes linearly. Accordingly, we consider regions where the

velocity is locally quadratic,

$$v = v_0 + \frac{\gamma_2'}{2} X_2^2, \tag{2.30}$$

where γ_2' is the magnitude of the shear-rate gradient and v_0 is an arbitrary local velocity that can be ignored since only velocity differences are significant. The corresponding magnitude of the shear rate and its gradient are given by

$$\dot{\gamma}_0 = \gamma_2' |X_2|, \quad \frac{\mathrm{d}\dot{\gamma}}{\mathrm{d}X_2} = \mathrm{sign}(X_2)\gamma_2'.$$
 (2.31*a,b*)

An example is the velocity field at the centre of planar Poiseuille flow in a channel of half-width H, where v is given by (2.1) with

$$v = v_0 \left[1 - \left(\frac{X_2}{H} \right)^2 \right]. \tag{2.32}$$

Here, v_0 is the velocity at centreline, $X_2 = 0$, and the magnitude of the shear rate is given by (2.31a,b) with $\gamma'_2 = 2v_0H^{-2}$. Neglecting Brownian motion in regions where the shear rate vanishes requires a more stringent condition; in this case, requirement (2.15) is replaced by

$$\frac{\gamma_2' a^3}{\mathcal{D}} \gg 1. \tag{2.33}$$

Inserting (2.31a,b) into (2.16) yields the relative velocity magnitude,

$$|v^{ij}| = \dot{\gamma}_2' |x_2^{-\infty}| |X_2 + X_2^{i, -\infty} + \frac{1}{2} x_2^{-\infty}|.$$
 (2.34)

For $|X_2| > X_c^{ij}$, the result reduces to the form of (2.18),

$$|v^{ij}| = \dot{\gamma}_2' |x_2^{-\infty}| (|X_2| + \text{sign}(X_2)[X_2^{i,-\infty} + \frac{1}{2}x_2^{-\infty}]), \quad |X_2| > X_c^{ij},$$
 (2.35)

where X_c^{ij} is an upper bound of the excluded region $|X_2^{i,-\infty} + \frac{1}{2}x_2^{-\infty}|$. Here, X_c^{ij} is given by

$$X_c^{ij} = \Delta X_{2,max}^{ij} + \frac{1}{2}r_c^{ij}, \tag{2.36}$$

where $\Delta X_{2,max}^{ij}$ is the maximum displacement magnitude of a type-i particle by a pair interaction with a type-j particle and is thus the upper bound for $|X_2^{i,-\infty}|$; the radius of the collision cross-section, r_c^{ij} , defined by (2.27a,b), is the upper bound for $|x_2^{-\infty}|$. In general, $\Delta X_{2,max}^{ij}$, and thus X_c^{ij} , are $O(r_c^{ij})$. For spherical particles that undergo contact interactions, $X_c^{ij} \leq r_c^{ij}$, as discussed in § 4.

For $|X_2| > X_c^{ij}$, the local analysis presented in § 2.3.1 applies with shear-rate magnitude and gradient given by (2.31*a,b*). Accordingly, a linearly varying diffusive flux and constant drift velocity are obtained according to (2.20)–(2.24). However, for $|X_2| < X_c^{ij}$, the relative velocity, v_{ij} , changes sign within the maximum range of particle displacements, $\Delta X_{2,max}^{ij}$, that contribute to the particle flux. Within this region, (2.34) must be used to describe the magnitude of the relative velocity. The use of (2.35) is inconsistent and leads to incorrect

results. For example, inserting the linearly varying diffusive flux balanced by the constant drift velocity, obtained by the local analysis (2.22)–(2.24) into (2.19) and then (2.10) yields,

$$X_2 n \frac{\mathrm{d}n}{\mathrm{d}X_2} = -M_1 n^2, \tag{2.37}$$

where M_1 is a positive constant. A singular distribution, $n \approx |X_2|^{-M_1}$ is thus obtained, as pointed out by Leighton & Acrivos (1987b).

The region $|X_2| < X_c^{ij}$ defines a boundary layer within which the transport coefficients exhibit a more complex dependence on position X_2 . By retaining the relative velocity magnitude (2.34) in this region, we obtain the essential dependence of the transport coefficients required to avoid the spurious singularity at $X_2 = 0$ without the need for any of the *ad hoc* manoeuvres used in prior studies, as discussed in the introduction.

Particle transport in the vorticity direction (k = 3) does not have a singular behaviour because there is no drift velocity, so the local analysis presented in § 2.3.1 is uniformly valid.

According to the derivation provided in Appendix A, the particle flux in the velocity-gradient direction is given by

$$F_{i2}(X_2) = F_{i2}^{(c)}(X_2) + F_{i2}^{(\dot{\gamma})}(X_2), \tag{2.38}$$

where the diffusive and drift fluxes are

$$F_{i2}^{(c)}(X_2) = -D_{i2}^s(X_2) \frac{\mathrm{d}n_i}{\mathrm{d}X_2} - \sum_{j=1}^m \left(D_{ij2}(X_2) \frac{\mathrm{d}n_j}{\mathrm{d}X_2} \right), \tag{2.39}$$

$$F_{i2}^{(\dot{\gamma})}(X_2) = -\gamma_2' n_{i0} V_i(X_2), \tag{2.40}$$

the diffusivities and drift-velocity coefficient are

$$D_{i2}^{s}(X_2) = \gamma_2'|X_2| \sum_{j=1}^{m} n_{j0}I_{ij}^{(1)}(X_2), \qquad (2.41)$$

$$D_{ij2}(X_2) = \gamma_2' |X_2| \, n_{i0} I_{ij}^{(2)}(X_2), \tag{2.42}$$

$$V_i(X_2) = \sum_{j=1}^{m} n_{j0} I_{ij}^{(3)}(X_2).$$
 (2.43)

Following the analysis presented in Appendix A, integrals $I_{ij}^{(1)}$, $I_{ij}^{(2)}$, $I_{ij}^{(3)}$ are given by

$$I_{ij}^{(1)}(X_2) = \frac{1}{|X_2|} \int_0^{\pi} \int_0^{r_c^{ij}} r^{-\infty} \sin \theta \left[\frac{1}{2} |X_2| (\Delta X_2^{ij})^2 B^2(X_2') + \frac{1}{3} (-\Delta X_2^{ij})^3 (1 - B^3(X_2')) + \frac{1}{4} r^{-\infty} \sin \theta (\Delta X_2^{ij})^2 (1 - B^2(X_2')) \right] r^{-\infty} dr^{-\infty} d\theta,$$
(2.44)

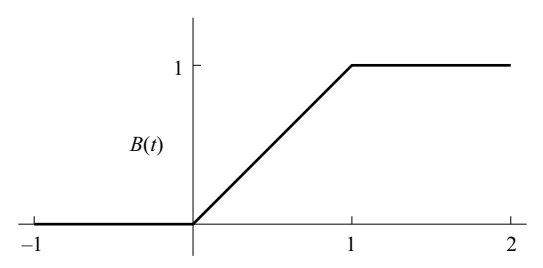


Figure 3. Ramp function defined by (2.48).

$$I_{ij}^{(2)}(X_2) = \frac{1}{|X_2|} \int_0^{\pi} \int_0^{r_c^{ij}} r^{-\infty} \sin \theta \left[r^{-\infty} \sin \theta |X_2| (-\Delta X_2^{ij}) B(X_2') + \frac{1}{2} |X_2| (\Delta X_2^{ij})^2 B^2(X_2') + \frac{1}{3} (-\Delta X_2^{ij})^3 (1 - B^3(X_2')) + \frac{3}{4} r^{-\infty} \sin \theta (\Delta X_2^{ij})^2 (1 - B^2(X_2')) + \frac{1}{2} (r^{-\infty} \sin \theta)^2 (-\Delta X_2^{ij}) (1 - B(X_2')) \right] r^{-\infty} dr^{-\infty} d\theta,$$
(2.45)

and

$$I_{ij}^{(3)}(X_2) = \operatorname{sign}(X_2) \int_0^{\pi} \int_0^{r_c^y} r^{-\infty} \sin \theta \left[\frac{1}{2} (\Delta X_2^{ij})^2 B^2(X_2') + \frac{1}{2} r^{-\infty} \sin \theta (-\Delta X_2^{ij}) B(X_2') + |X_2| (-\Delta X_2^{ij}) (1 - B(X_2')) \right] r^{-\infty} dr^{-\infty} d\theta,$$
(2.46)

where $(r^{-\infty}, \theta)$ are the cylindrical coordinates defined in figure 2, and

$$X_2' = \frac{|X_2| - \frac{1}{2}r^{-\infty}\sin\theta}{-\Delta X_2^{ij}}. (2.47)$$

Here, B(t) is the ramp function sketched in figure 3 and defined by

$$B(t) = t\Theta(t) - (t-1)\Theta(t-1),$$
 (2.48)

where $\Theta(t)$ is the Heaviside function. Note that

$$-\Delta X_2^{ij} > 0 \quad \text{for } 0 < r^{-\infty} < r_c^{ij}, \quad 0 < \theta < \pi, \tag{2.49}$$

by (2.9) and the remark below it. It follows that integrals (2.44)–(2.46), and thus the transport coefficients (2.41)–(2.43), are positive provided $X_2 \neq 0$.

2.3.3. Discussion

Here, we point out the salient features of the diffusive and drift fluxes in the boundary-layer region.

For $|X_2| \ge X_c^{ij}$, we have $X_2' \ge 1$, according to (2.36) and (2.47), and thus

$$B(X_2') = 1. (2.50)$$

Inserting this result into integrals (2.44)–(2.46) reduces them to their local forms

$$I_{ij}^{(1)} \to I_{ij2}^A, \quad I_{ij}^{(2)} \to I_{ij2}^A + I_{ij2}^B, \quad I_{ij}^{(3)} \to \operatorname{sign}(X_2)(I_{ij2}^A + \frac{1}{2}I_{ij2}^B), \quad |X_2| \ge X_c^{ij}. \quad (2.51a-c)$$

Accordingly, the transport coefficients (2.41)–(2.43) reduce to their corresponding local forms, (2.22)–(2.24), with the shear-rate magnitude and its gradient given by (2.31a,b).

First-derivative discontinuities introduced by the ramp function (2.48) are manifest by second-derivative discontinuities of integrals $I_{ij}^{(k)}(X_2)$ (k = 1, 2, 3) and the transport coefficients (2.41)–(2.43) at $|X_2| = X_c^{ij}$. The source of these discontinuities is the discrete interaction range (2.27a,b) for contact interactions between spherical particles.

According to (2.44)–(2.46), integrals $I^{(1)}(X_2)$ and $I^{(2)}(X_2)$ are even functions of X_2 and $I^{(3)}(X_2)$ is an odd function. (This is plainly seen in the antecedent (A2)–(A4).) Thus, diffusivities (2.41)–(2.42) are even functions and drift velocities (2.43) are odd functions of X_2 . Near the centreline, integrals (2.44)–(2.46) reduce to

$$\lim_{X_{2}\to 0} |X_{2}| I_{ij}^{(1)}(X_{2}) = \int_{0}^{\pi} \int_{0}^{r_{c}^{ij}} r^{-\infty} \sin \theta \left[\frac{1}{3} (-\Delta X_{2}^{ij})^{3} + \frac{1}{4} r^{-\infty} \sin \theta \left(\Delta X_{2}^{ij} \right)^{2} \right] r^{-\infty} dr^{-\infty} d\theta, \qquad (2.52)$$

$$\lim_{X_{2}\to 0} |X_{2}| I_{ij}^{(2)}(X_{2}) = \int_{0}^{\pi} \int_{0}^{r_{c}^{ij}} r^{-\infty} \sin \theta \left[\frac{1}{3} (-\Delta X_{2}^{ij})^{3} + \frac{3}{4} r^{-\infty} \sin \theta (\Delta X_{2}^{ij})^{2} + \frac{1}{2} (r^{-\infty} \sin \theta)^{2} (-\Delta X_{2}^{ij}) \right] r^{-\infty} dr^{-\infty} d\theta, \qquad (2.53)$$

and

$$\lim_{X_2 \to 0} I_{ij}^{(3)}(X_2) = X_2 \int_0^{\pi} \int_0^{r_c^{ij}} r^{-\infty} \sin \theta (-\Delta X_2^{ij}) r^{-\infty} dr^{-\infty} d\theta.$$
 (2.54)

Inserting these results with (2.49) into (2.41)–(2.43) shows that diffusivities are finite and positive and drift velocities are linear with positive slope for $X_2 \rightarrow 0$. Inserting these results into (2.38) and (2.10) indicates that particle transport near the centreline is governed by

$$n - dy = -M_2 y n^2, \quad |y| \to 0,$$
 (2.55)

where M_2 is a positive constant, and $y = X_2/X_c^{ij}$ is a dimensionless length variable. By contrast to (2.37), this equation predicts the smooth, non-singular behaviour, $n \approx n_0(1 - \frac{1}{2}M_2 y^2)$, where n_0 is the number density at y = 0. Hence, the source of the classical singular particle distribution, described above, is eliminated. Note that X_c^{ij} introduces a particle-related length scale on the distribution near the centreline, whereas (2.37) describes a distribution without a length scale.

Rivera *et al.* (2016) accommodated the non-vanishing diffusivities at the centreline but ignored variations in the drift velocity. This led to the prediction of a linear cusp at the centreline, as seen by inserting (41) from their paper into (2.10) to obtain

$$n\frac{\mathrm{d}n}{\mathrm{d}\tilde{y}} = -M_3 \operatorname{sign}(\tilde{y})n^2, \quad |y| \to 0, \tag{2.56}$$

which yields $n \approx n_0(1 - M_3|\tilde{y}|)$, consistent with the result shown in figure 10 of their paper. Here, M_3 is a positive constant, and $\tilde{y} = X_2/H$.

The diffusive flux model (Phillips *et al.* 1992) also predicts a linear cusp at the centreline, except with $n_0 = n_m$, corresponding the maximum packing fraction, as shown

in Appendix B. Although the diffusive flux model uses local coefficients for diffusivity and drift velocity in the particle transport equation (B1), the singular behaviour (2.37) is avoided through the use of a suspension viscosity model that diverges at a prescribed maximum packing fraction.

3. Stationary particle distributions: general results

The results presented in this section are independent of the character of pairwise particle interactions. Specific results for particles that undergo short-range contact interactions are presented in § 5.

3.1. Non-vanishing shear rates

Here, we present an exact stationary solution for the particle distribution in a polydisperse suspension in a flow with a power-law shear-rate magnitude,

$$\dot{\gamma} = C_1 X_2^{\beta},\tag{3.1}$$

where β and C_1 are arbitrary non-zero constants and $X_2 > 0$ is assumed. Accordingly, the shear rate is non-vanishing (and non-singular).

Inserting (2.19)–(2.24) into (2.10) yields

$$\sum_{i=1}^{m} (\dot{\gamma} [I_{ij2}^{A} n_{j} n_{i}' + (I_{ij2}^{A} + I_{ij2}^{B}) n_{i} n_{j}'] + \dot{\gamma}' [n_{i} n_{j} (I_{ij2}^{A} + \frac{1}{2} I_{ij2}^{B})]) = 0,$$
 (3.2)

for i = 1, 2, ..., m, where primes are used to denote X_2 -derivatives.

A power-law particle distribution

$$n_i(X_2) = c_i X_2^{-\beta/2} \tag{3.3}$$

is seen to satisfy (3.2) with arbitrary coefficients c_i . This is a general result that holds independent of the details of pairwise particle interactions in a given system. There are two features that should be noted here: (i) the effect of particle interactions exactly cancel, i.e. the spatial distribution of each particle species is unaffected by the presence of the others, and (ii) particle size does not affect the particle distribution. These features break down in regions where the shear rate vanishes, as seen below.

3.2. Planar Poiseuille flow

Here, we consider the steady-state particle distribution in quadratic flows (2.30), including regions $X_2 \rightarrow 0$, where the shear rate vanishes.

3.2.1. Polydisperse suspension

Inserting (2.38)–(2.43) into (2.10) yields the equation governing the stationary particle distribution

$$\sum_{i=1}^{m} (|X_2|[I_{ij}^{(1)}(X_2)n_j n_i' + I_{ij}^{(2)}(X_2)n_i n_j'] + I_{ij}^{(3)}(X_2)n_i n_j) = 0, \quad |X_2| < X_c,$$
(3.4)

for i = 1, 2, ..., m. In a polydisperse system, each binary interaction has a distinct boundary-layer half-thickness, X_c^{ij} , determined by (2.36), and X_c is the maximum of these,

i.e.

$$X_c = \sup\{X_c^{ij}\}. \tag{3.5}$$

For $|X_2| > X_c$, (3.4) reduces to (3.2), according to (2.51*a*–*c*), thus particle distributions are decoupled and obey distribution (3.3) with $\beta = 1$, i.e.

$$n_i(X_2) = n_{ic} X_c^{1/2} |X_2|^{-1/2}, \quad |X_2| > X_c,$$
 (3.6)

where n_{ic} is the number density of species i at $X_2 = X_c$.

The spatial distributions of particle species are coupled for $|X_2| < X_c$. By contrast to the scale-free power-law distribution (3.3) that governs particle distributions in regions of non-vanishing shear rate, the coupling that occurs in regions of vanishing shear rate imposes a particle-related length scale X_c . A dimensionless coordinate is thus introduced using the length scale X_c

$$y = X_2/X_c. (3.7)$$

It will also be useful to define the dimensionless number densities

$$\bar{n}_i = n_i/n_c, \quad \bar{N}_i = n_i/n_{ic},$$
 (3.8*a*,*b*)

where n_{ic} is the number density of particle species i at $X_2 = X_c$ and $n_c = \sum_{i=1}^m n_{ic}$. In terms of these variables, (3.4) becomes

$$\sum_{i=1}^{m} (D_{ij}^{(1)}(y)\bar{n}_j\bar{n}_i' + D_{ij}^{(2)}(y)\bar{n}_i\bar{n}_j' + V_{ij}(y)\bar{n}_i\bar{n}_j) = 0, \quad |y| < 1,$$
(3.9)

where primes denote y-derivatives and dimensionless transport coefficients are defined

$$D_{ij}^{(k)}(y) = |y|I_{ij}^{(k)}(y), \quad k = 1, 2; \quad V_{ij}(y) = I_{ij}^{(3)}(y). \tag{3.10a,b}$$

Boundary conditions for (3.9) are given by

$$\bar{n}_i(1) = x_{ic},$$
 (3.11)

where $x_{ic} = n_{ic}/n_c$ is the number density fraction at y = 1. Outside of the coupled boundary-layer region, |y| > 1, the dimensionless particle densities are given by

$$\bar{N}_i(y) = |y|^{-1/2},$$
 (3.12)

according to (3.6).

The number densities n_{ic} at y = 1 are related to the prescribed bulk number densities $n_{i\infty}$, through the conservation constraint (2.11), which in this case becomes

$$qn_{i\infty} = \int_0^H v(x)n_i(x) \, \mathrm{d}x,\tag{3.13}$$

for i = 1, ..., m, where v(x) is the velocity (2.32), $q = \frac{2}{3}v_0H$ is the corresponding volume flux per unit depth and H is the half-width of the channel. Using dimensionless variables and (3.12) yields

$$\bar{n}_{i\infty} = \frac{12}{5} \epsilon^{1/2} x_{ic} (1 - \frac{5}{8} \epsilon^{1/2} \Delta \bar{N}_i) + O(\epsilon^{5/2}),$$
 (3.14)

where $\bar{n}_{i\infty} = n_{i\infty}/n_c$ and

$$\epsilon = X_c/H,\tag{3.15}$$

is the ratio of the two length scales that affect the particle distributions. Under the assumption that the channel width is large compared with the particle size, $\epsilon \ll 1$. The

quantity $\Delta \bar{N}_i$ is the (average) deficit of type-*i* particle density in the centre region compared with the singular distribution (3.12)

$$\Delta \bar{N}_i = \int_0^1 [y^{-1/2} - \bar{N}_i(y)] \, \mathrm{d}y, \tag{3.16}$$

where \bar{N}_i is defined above. This particle deficit results from the modified transport coefficients in the region |y| < 1. The $O(\epsilon^{5/2})$ error in (3.14) results from neglecting particle—wall interactions. Dividing (3.14) by its sum over all species provides a relation between the composition at $X_2 = X_c$ and the bulk composition

$$x_{i\infty} = x_{ic} \left(\frac{1 - \frac{5}{8} \epsilon^{1/2} \Delta \bar{N}_i}{1 - \frac{5}{8} \epsilon^{1/2} \sum_{j=1}^{m} x_{jc} \Delta \bar{N}_j} \right) + O(\epsilon^2), \tag{3.17}$$

for $i=1,\ldots,m-1$, where $x_{i\infty}=n_{i\infty}/n_{\infty}$ is the prescribed bulk number fraction of species i. This result in combination with (3.11) provides the boundary conditions for (3.4). In wide channels, $\epsilon \ll 1$, the composition in the centre region is insensitive to channel width; at leading order, (3.17) yields $x_{ic} \approx x_{i\infty}$ and boundary conditions for (3.4) simplify to

$$\bar{n}_i(1) = x_{i\infty}. (3.18)$$

Dividing $\bar{n}_i(y)$ by (3.14) yields the particle distributions normalized by their bulk number densities,

$$\frac{n_i(y)}{n_{i\infty}} = f_i(\epsilon)\bar{N}_i(y), \tag{3.19}$$

where

$$f_i(\epsilon) = \frac{\frac{5}{12}\epsilon^{-1/2}}{1 - \frac{5}{8}\epsilon^{1/2}\Delta\bar{N}_i}.$$
 (3.20)

Outside the centre region, this distribution reduces to

$$\frac{n_i(\tilde{y})}{n_{i\infty}} = \frac{5}{12} \tilde{y}^{-1/2} \left(1 - \frac{5}{8} \epsilon^{1/2} \Delta \bar{N}_i \right)^{-1} + O(\epsilon^2), \quad |y| > 1, \tag{3.21}$$

according to (3.12), where $\tilde{y} = X_2/H$. The result indicates that the channel width sets the length scale of the distribution for |y| > 1.

3.2.2. Monodisperse particle distribution

For a single particle species, (3.9)–(3.11) reduce to the linear boundary value problem

$$D(y)\bar{N}' + V(y)\bar{N} = 0, \quad \bar{N}(1) = 1,$$
 (3.22)

where \bar{N} is defined by (3.8b) and the index i is dropped to distinguish the monodisperse case. The transport coefficients are given by

$$D(y) = D_{11}^{(1)}(y) + D_{11}^{(2)}(y), \quad V(y) = V_{11}(y). \tag{3.23a,b}$$

The solution of boundary value problem (3.22) is

$$\bar{N}(y) = \exp\left(\int_{|y|}^{1} \frac{V(t)}{D(t)} dt\right). \tag{3.24}$$

For |y| > 1, the transport coefficients (3.23*a*,*b*) reduce to their local forms

$$D(y) = |y|(2I_{112}^A + I_{112}^B), \quad V(y) = \operatorname{sign}(y)(I_{112}^A + \frac{1}{2}I_{112}^B), \tag{3.25a,b}$$

and thus V(y)/D(y) = 1/2y, according to (2.51a-c), so that the outer solution (3.12) is recovered. Given that D(y) is non-vanishing and V(y) vanishes linearly for $|y| \to 0$, as discussed in § 2.3.3, it follows that \bar{N} has a maximum with $d\bar{N}/dy = 0$ at y = 0, consistent with the scaling predicted by (2.55). From the continuity of D(y) and V(y) up to their second derivatives at |y| = 1, it follows that $\bar{N}(y)$ is continuous up to its third derivative.

From (3.19), we have

$$\frac{n(y)}{n_{\infty}} = f(\epsilon)\bar{N}(y), \tag{3.26}$$

where $\bar{N}(y)$ is given by (3.24), $\Delta \bar{N}$ given by

$$\Delta \bar{N} = \int_0^1 \left[y^{-1/2} - \exp\left(\int_{|y|}^1 \frac{V(t)}{D(t)} \, dt \right) \right] dy, \tag{3.27}$$

and

$$f(\epsilon) = \frac{\frac{5}{12}\epsilon^{-1/2}}{1 - \frac{5}{8}\epsilon^{1/2}\Delta\bar{N}}.$$
 (3.28)

3.2.3. Superposition approximation

The particle distribution in a polydisperse mixture with weak interactions between particles of different sizes can be approximated by a superposition of monodisperse distributions for each particle size (or size class).

Displacements resulting from collisions between particles of different sizes are usually smaller than displacements resulting from collisions between equal-size particles. This is true for particles that undergo contact interactions, as discussed in § 4.2, because collision rates diminish rapidly with size ratio (Adler 1981; Wang, Zinchenko & Davis 1994; Reboucas & Loewenberg 2021b). Thus, the superposition approximation may be expected to hold for particles with vastly different sizes. It may be also expected to hold for similar-size particles because the effect is similar to increasing the total number density and the latter scales out of the equations, as explained in § 2.2.1. The superposition approximation is further supported by the fact that particle distributions are coupled only in the boundary layer; outside the boundary-layer particle distributions are decoupled, as shown in § 3.1.

According to the superposition approximation, distribution (3.19) reduces to

$$\frac{n_i(y_i)}{n_{i\infty}} \simeq f(\epsilon_i)\bar{N}(y_i), \tag{3.29}$$

for $i = 1, \ldots, m$. Here,

$$y_i = X_2/X_c^{ii}$$
 and $\epsilon_i = X_c^{ii}/H$, (3.30*a*,*b*)

where $\bar{N}(y_i)$, $\Delta \bar{N}$ and f(x) are given by (3.24) and (3.27) and (3.28); X_c^{ii} is the boundary-layer thickness for a suspension of type-i particles. The result reduces to the monodisperse distribution (3.26) by dropping the index i.

Comparing (3.19) and (3.29) indicates that the superposition approximation is equivalent to $\epsilon^{-1/2}\bar{N}_i(y_i) \simeq \epsilon_i^{-1/2}\bar{N}(y_i)$ and $\epsilon^{1/2}\Delta\bar{N}_i \simeq \epsilon_i^{1/2}\Delta\bar{N}$ and, thus,

$$\bar{N}_i(y_i) \simeq \chi_i^{-1/2} \bar{N}(y_i), \quad \Delta \bar{N}_i \simeq \chi_i^{1/2} \Delta \bar{N},$$
 (3.31*a,b*)

where χ_i is the ratio

$$\chi_i = X_c^{ii} / X_c, \tag{3.32}$$

and $\chi_i \leq 1$, according to (3.5).

Under the assumption that X_c^{ii} scales with particle size, the above results predict that particle segregation occurs in the boundary layer region with relative enrichment of smaller particles. The dependence of the centreline particle density on particle size is described by the function $f(\epsilon_i)$. According to (3.28), particle densities at the centreline scale approximately with the inverse square root of particle size, assuming that particles are small compared with channel width, $\epsilon_i \ll 1$. Distributions of smaller particles adhere more closely to the singular outer distribution (3.12) as reflected by their smaller average density deficit (3.16), according to (3.31b).

The error of the superposition approximation, resulting from interactions between particles of different sizes in the boundary layer, is characterized by the polydisperse enrichment

$$\Delta \bar{N}_{ij} = \int_0^1 [\bar{N}_i(y) - \chi_i^{-1/2} \bar{N}(y/\chi_i)] \, \mathrm{d}y, \tag{3.33}$$

where $\bar{N}_i(y)$ is the exact distribution for type-*i* particles in a polydisperse suspension and $\chi_i^{-1/2}\bar{N}(y_i)$ is superposition approximation (3.31*a*). According to (3.16) and (3.31*b*), we have the relation $\Delta \bar{N}_i = \chi^{1/2} \Delta \bar{N} - \Delta \bar{N}_{ii}$.

4. Particle displacements

4.1. Contact interactions

Spherical particles that undergo short-range symmetry-breaking 'contact' interactions in shear flow are considered here, specifically, particles with surface roughness, permeable particles and emulsion drops. Pair trajectories of such particles are analytically integrated to yield formulas for binary cross-stream particle displacements ΔX_k^{12} , ΔX_k^{21} (k=2,3) involving integrals of the standard pair mobility functions for spherical particles. Note that superscripts 1 and 2 are used in this section to refer to particle labels, not particle species, by contrast to the superscripts i and j introduced earlier. Accordingly, ΔX_k^{12} refers to the net displacement of particle-1 resulting from its collision with particle-2 and *vice versa* for ΔX_k^{21} , whereas ΔX_k^{ij} is the net displacement of any type-i particle resulting from its collision with any type-j particle. Similarly, we will use r_c to denote the collision cross-section for particles 1 and 2, by contrast with the quantity r_c^{ij} , defined by (2.27a,b), that refers to the collision cross-section for any type-i and j particles. The particles have radii a_1 and a_2 , and size ratio $\kappa = a_2/a_1$. We assign label 1 to the larger particle thus, only $\kappa \leq 1$ needs consideration.

Recall that the particles are assumed to be non-Brownian and neutrally buoyant. Here, creeping flow conditions are assumed, and particle inertia is neglected

4.1.1. Rough particles

According to the usual model for rough particles, surface asperities with size d transmit a normal inter-particle contact force between rigid particles that prevents surface-to-surface particle separations less than d but do not exert a tensile force upon separation. Here, $\delta = d/\bar{a}$ is the dimensionless roughness amplitude, $\bar{a} = (a_1 + a_2)/2$ is the average particle radius and $\bar{\delta} \ll 1$ is assumed. Models for rough particles may also include a coefficient of friction to describe tangential forces transmitted by surface asperities at contact, $h_0 = d$; the limiting cases of frictionless or tangentially locking particle contacts are most often used (Smart *et al.* 1993; da Cunha & Hinch 1996; Rampall *et al.* 1997; Wilson 2005).

4.1.2. Permeable particles

Particle permeability is another short-range, symmetry-breaking mechanism. The dimensionless permeability is defined $\bar{K}=k/\bar{a}^2$, where k is the permeability and Darcy's law is used to describe the intraparticle flow. Weak permeability alleviates the lubrication pressure between particles, allowing particle contact, $h_0=0$, but otherwise has little effect on the pair interaction. Under the assumption that the particles are rigid and not cohesive, the effect of weak permeability closely resembles small-amplitude particle roughness. The following hydrodynamic equivalence between particle roughness and particle permeability was proposed based on the contact time between particles under the action of a constant force (Reboucas & Loewenberg 2021a):

$$\bar{\delta} \longleftrightarrow 0.7224 \nu^{1/5} \bar{K}^{2/5},\tag{4.1}$$

where $\bar{\delta}$ and \bar{K} are the dimensionless particle roughness and permeability, and $\nu = 2\kappa/(1+\kappa)^2$. This relation is based on the assumption that no-slip boundary conditions apply on the particle surfaces. This correlation has been shown to hold accurately for colliding pair trajectories in several types of flow (including shear) for a wide range of size ratios and permeabilities (Reboucas & Loewenberg 2021b).

4.1.3. Non-coalescing spherical drops

The small, flattened thin film that forms in the near-contact region between approximately spherical emulsion drops in apparent contact, $h_0 \approx 0$, under small-deformation conditions is a third short-range mechanism that breaks the symmetry of pair trajectories. Drop deformation is principally controlled by the capillary number, $Ca = \mu \dot{\gamma} a/\sigma$, where μ is the viscosity of the continuous-phase fluid, $\dot{\gamma}$ is the magnitude of the local shear rate, a is the drop radius and σ is surface tension; small-deformation conditions are characterized by $Ca \ll 1$.

In the absence of van der Waals attraction, slow drainage from the film (Nemer *et al.* 2004; Zinchenko & Davis 2005; Nemer *et al.* 2007; Santoro & Loewenberg 2009; Nemer *et al.* 2013) prevents drop coalescence in the compressional quadrant of the flow that would otherwise result between spherical drops (i.e. infinite surface tension) with tangentially mobile interfaces (Zinchenko 1978; Wang *et al.* 1994). The film quickly reverts as the drops rotate into the extensional quadrant of the flow and has little effect on their separation (Zinchenko 1984; Loewenberg & Hinch 1997).

The foregoing discussion indicates that $Ca \to 0$ is a singular limit: spherical drops, characterized by Ca = 0, undergo coalescence in shear flow for trajectories with sufficiently small offsets, but coalescence does not occur for Ca > 0. Non-coalescing spherical drops is a rigorous description for the pair interactions of drops in the small-deformation limit, $Ca \to 0$, and absence of van der Waals attraction. Hydrodynamic

interactions are described by the mobility functions for spherical drops (Zinchenko 1978), augmented by an inter-particle force at contact, $h_0 = 0$, that acts along the line of centres and only in compression, preventing overlap in the compressional quadrant of the flow, but otherwise having no effect. According to this description, hydrodynamic interactions depend on size ratio and the drop- to continuous-phase viscosity ratio, λ , but are independent of the capillary number.

Non-coalescing spherical drops is a model for pair interactions of drops and other deformable particles under small-deformation conditions. Its predictions for drop displacements in shear flow are supported by the boundary integral simulations of Loewenberg & Hinch (1997) for drops under finite-capillary-number conditions, where drop displacements were shown to be a weak function of *Ca* and the predictions of non-coalescing spherical drops were shown to be in approximate agreement with exact simulations even for moderate capillary numbers (Loewenberg & Hinch 1997). Boundary integral simulations of capsules and red blood cells also show an insensitivity to deformation for moderate capillary numbers (Pranay *et al.* 2010; Kumar & Graham 2011; Omori *et al.* 2013; Qi & Shaqfeh 2017), suggesting that a similar simplified model may provide a good approximation.

4.2. Trajectories of particles with contact interactions

Relative particle trajectories emanate from $x_1 \to -\infty$ for $x_2^{-\infty} > 0$ and from $x_1 \to +\infty$ for $x_2^{-\infty} < 0$. Apart from the contact interactions, trajectories are accurately described using standard pair mobility functions for spherical particles (or drops) in shear flow (Batchelor & Green 1972a; Zinchenko 1978, 1980, 1983). Accordingly, particles with short-range binary contact interactions have circular upstream collision cross-sections, defined by (2.27a,b), where r_c depends on size ratio, and on the roughness, permeability, or drop- to continuous-phase viscosity ratio, respectively, for rough or permeable particles or drops. Collision cross-sections, or equivalently collision efficiencies $E_{12} = (r_c/(2\bar{a}))^3$, are available in the literature for rough and permeable particles and drops (Wang *et al.* 1994; Reboucas & Loewenberg 2021b). Trajectories with offsets $r^{-\infty} > r_c$ are reversible, i.e. $\Delta X_k^{12} = \Delta X_k^{21} = 0$.

Pair trajectories with upstream trajectory offsets, $r^{-\infty} < r_c$, reach the contact surface, defined by $s = s^*$, where $s = r/\bar{a}$ is the centre-to-centre separation, r, normalized by the average particle radius. For permeable particles and drops, $s^* = 2$; for particles with surface roughness, $s = 2 + \bar{\delta}$. On the contact surface, the particles undergo relative rotation through the compressional quadrant of the flow and separate at the equator $(x_1 = 0)$, under the assumption that cohesive forces are absent. The motion on the contact surface is described by a subset of the trajectory equations corresponding to zero relative radial velocity. Examples of contacting trajectories are shown in figures 4 and 5.

Below a critical roughness, the collision cross-section for rough particles vanishes; similarly, there exists a critical permeability below which $r_c = 0$. The values of these critical parameters increase with diminishing size ratio (Arp & Mason 1977; Reboucas & Loewenberg 2021b). Likewise, drops have a critical viscosity ratio beyond which $r_c = 0$, and the critical viscosity ratio decreases with diminishing size ratio (Wang *et al.* 1994). Equivalently, there exists a finite critical size ratio ratio, κ^* , below which $r_c = 0$ for fixed values of particle roughness or permeability, or drop viscosity ratio.

4.2.1. *Maximum particle displacements*

Maximum particle displacements are important because they determine the thickness of the boundary layer that forms in regions of vanishing shear rate. Maximum displacement

R.B. Reboucas, A.Z. Zinchenko and M. Loewenberg

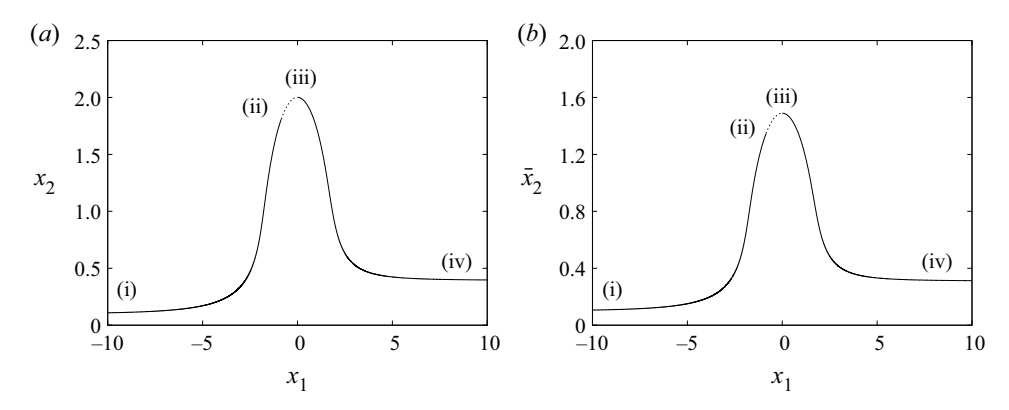


Figure 4. Relative (a) and pair (b) particle trajectories in velocity-gradient plane, size ratio $\kappa = a_2/a_1 = 1/2$, roughness $\bar{\delta} = d/\bar{a} = 10^{-3}$; initial positions (i), contact surface (ii)–(iii) (dotted lines), final positions (iv). Relative $x = X^{(2)} - X^{(1)}$ and pair $\bar{x} = X^{(1)} + X^{(2)}$ coordinates of particles non-dimensionalized by the average radius $\bar{a} = \frac{1}{2}(a_1 + a_2)$; initial conditions $x = (-\infty, 0.1, 0)$ and $\bar{x} = (-\infty, 0.1, 0)$.

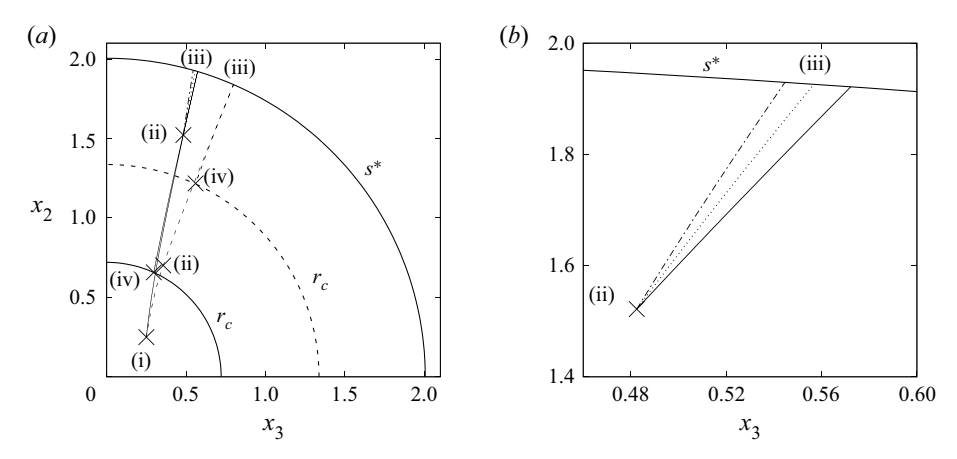


Figure 5. Offset relative trajectory shown in cross-flow plane (a) and enlargement (b), size ratio $\kappa = a_2/a_1 = 1/2$; particles with roughness $\bar{\delta} = d/\bar{a} = 5 \times 10^{-3}$, frictionless contact (solid lines), infinite contact friction coefficient (dash-dotted lines); permeable particles $\bar{K} = 6 \times 10^{-6}$ from (4.1) (dotted lines); drops with viscosity ratio $\lambda = 1$ (dashed lines); initial offset (i), contact surface (ii)–(iii), final offset (iv); collision surface s^* (large circle), collision cross-sections r_c particles (small circle), drops (dashed circle). Relative $x = X^{(2)} - X^{(1)}$ coordinates of particles non-dimensionalized by the average radius $\bar{a} = \frac{1}{2}(a_1 + a_2)$; initial conditions $x = (-\infty, 0.25, 0.25)$.

magnitudes in the X_2 -direction are achieved for $r^{-\infty} \to 0$ with $\theta = \pm \pi/2$ (i.e. $x_3^{-\infty} = 0$). For contact interactions between pairs of inertialess particles in creeping flows, the maximum displacement magnitudes satisfy

$$\Delta X_{2,max}^{12} + \Delta X_{2,max}^{21} = r_c, \tag{4.2}$$

and for equal-size particles,

$$\Delta X_{2,max}^{12} = \Delta X_{2,max}^{21} = \frac{1}{2}r_c, \quad \kappa = 1,$$
 (4.3*a,b*)

by symmetry.

Bounds for the magnitudes of individual displacements of unequal size particles are given by

$$0 < \Delta X_{2,max}^{12} \le \frac{1}{2}r_c, \quad \frac{1}{2}r_c \le \Delta X_{2,max}^{21} < r_c, \quad 0 < \kappa \le 1, \tag{4.4a-c}$$

and for extreme size ratios,

$$\Delta X_{2,max}^{12} \rightarrow 0$$
, $\Delta X_{2,max}^{21} \rightarrow r_c$, $\kappa \rightarrow 0$. (4.5*a*-*c*)

In Appendix C, particle trajectories, and net displacements, ΔX_k^{12} and ΔX_k^{21} , are expressed in terms of formulas involving quadratures of pair mobility functions for spherical particles. Results for particle displacements are used to determine particle distributions in § 5. Examples of particle trajectories, and particle displacements are shown here and discussed.

4.3.1. Effects of friction and permeability

Contact friction can affect the relative motion of rough particles in contact. As explained in § C.4, it enhances particle displacements in the X_2 -direction and suppresses them in the X_3 -direction. This behaviour is supported by computations of self- and gradient diffusivities (2.22) and (2.23) of equal-size particles by da Cunha & Hinch (1996) for the limiting cases of frictionless and tangentially locking particle contacts, i.e. the latter produced larger diffusivities in the X_2 -direction and smaller in the X_3 -direction. Similar results were obtained for the two limiting cases, however.

An example of relative trajectories for the limiting cases of frictionless and tangentially locking particle contacts are contrasted in figure 5 (solid and dash-dotted lines) for size ratio $\kappa = 1/2$. Very similar trajectories are obtained for the two cases but the enlargement shown in panel (b) of the figure concurs that friction enhances particle displacement in the X_2 -direction and suppresses it in the X_3 -direction. The insensitivity to contact friction seen here and in the results of da Cunha & Hinch (1996) indicate that lubrication resistance dominates the effect of friction. Contact friction was neglected for all other rough particle calculations presented herein.

The trajectory for permeable particles depicted by the dotted line in figure 5(b) lies between the two trajectories for rough particles, corresponding to the limiting cases of contact friction. This example illustrates a general result explained in § C.4.1. The displacements of permeable particles lie between the results for rough particles with frictionless and tangentially locking particle contacts and roughness prescribed by (4.1). These limits provide tight bounds on displacements of permeable particles inasmuch as rough particle displacements are insensitive to contact friction.

This finding and the reliability of correlation (4.1) on colliding trajectories that terminate on the contact surface discussed in § 4.1.2 supports its use for contacting trajectories in their entirety. It follows that pair displacements and thus transport of permeable particles can be reliably predicted from results for rough particles with either frictionless or tangentially locking particle contacts using (4.1).

4.3.2. Particle displacements

Examples of net particle displacements for unequal size rough particles and drops in the velocity-gradient and vorticity directions are shown by the contour maps in figures 6 and 7. Figures 8 and 9 show the collision cross-section (and maximum displacement) for

R.B. Reboucas, A.Z. Zinchenko and M. Loewenberg

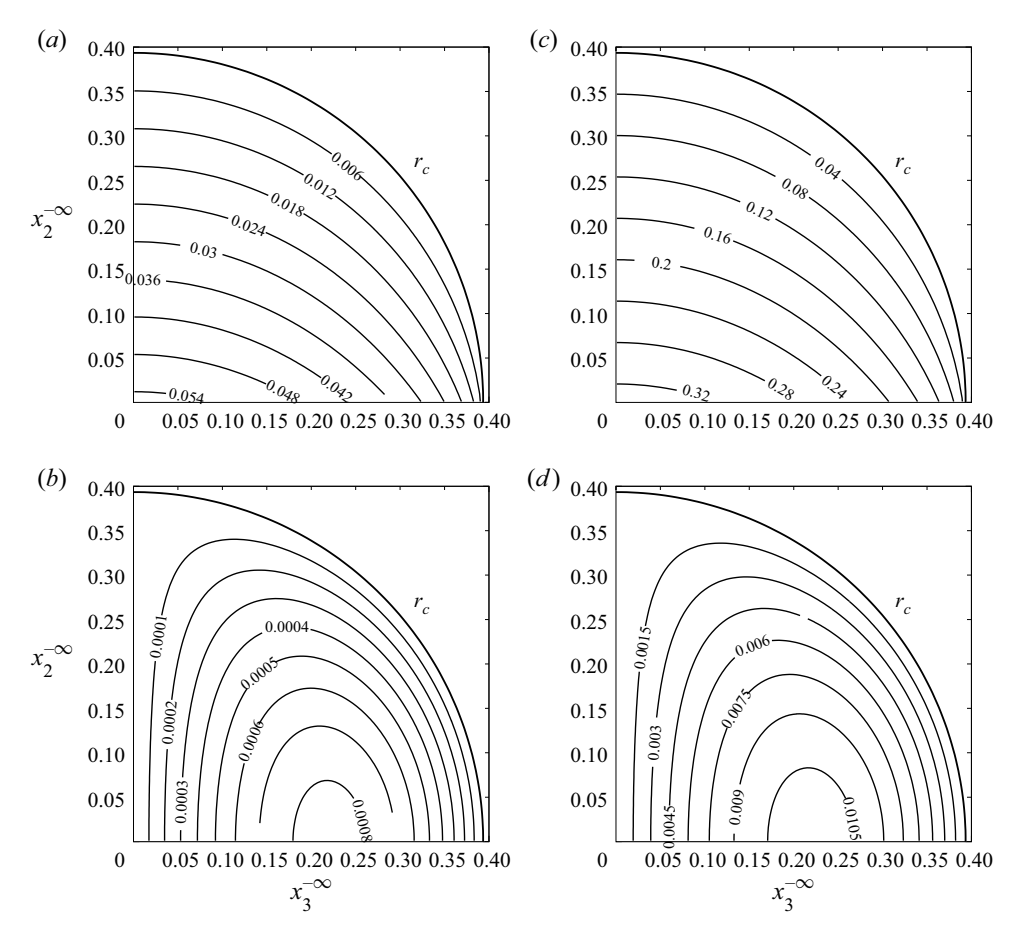


Figure 6. Displacement magnitudes of (a) larger and (b) smaller particles in velocity-gradient direction, and (c) larger and (d) smaller particles in vorticity direction; size ratio $\kappa = a_2/a_1 = 1/2$, roughness $\bar{\delta} = d/\bar{a} = 10^{-3}$. Displacements and cross-flow coordinates non-dimensionalized by the average radius, $\bar{a} = \frac{1}{2}(a_1 + a_2)$; radius of collision cross-section, r_c , indicated by outermost quarter circle. By the symmetry relations (2.7) and (2.8a,b), only a quarter of the cross-flow plane is shown.

equal-size particles as functions of particle roughness and drop viscosity. Figures 10 and 11 show maximum particle displacements as a function of size ratio, illustrating relations (4.2)–(4.5a–c).

The results in figures 5–11 illustrate that (i) particle displacements in the velocity-gradient direction are considerably larger than in the vorticity direction, especially for rough particles, and (ii) pair collisions displace the smaller particle much more than the larger, even for modest size ratios (beyond the critical value).

4.4. Boundary-layer thickness

Given that maximum displacements (4.2) occur for $r^{-\infty} \to 0$ and given $\Delta X_2^{12} = \Delta X_2^{21} = 0$ for $r^{-\infty} = r_c$, suggests that (2.36) can be replaced by the tighter bound

$$X_c^{ij} = max(\Delta X_{2,max}^{ij}, \frac{1}{2}r_c^{ij}),$$
 (4.6)

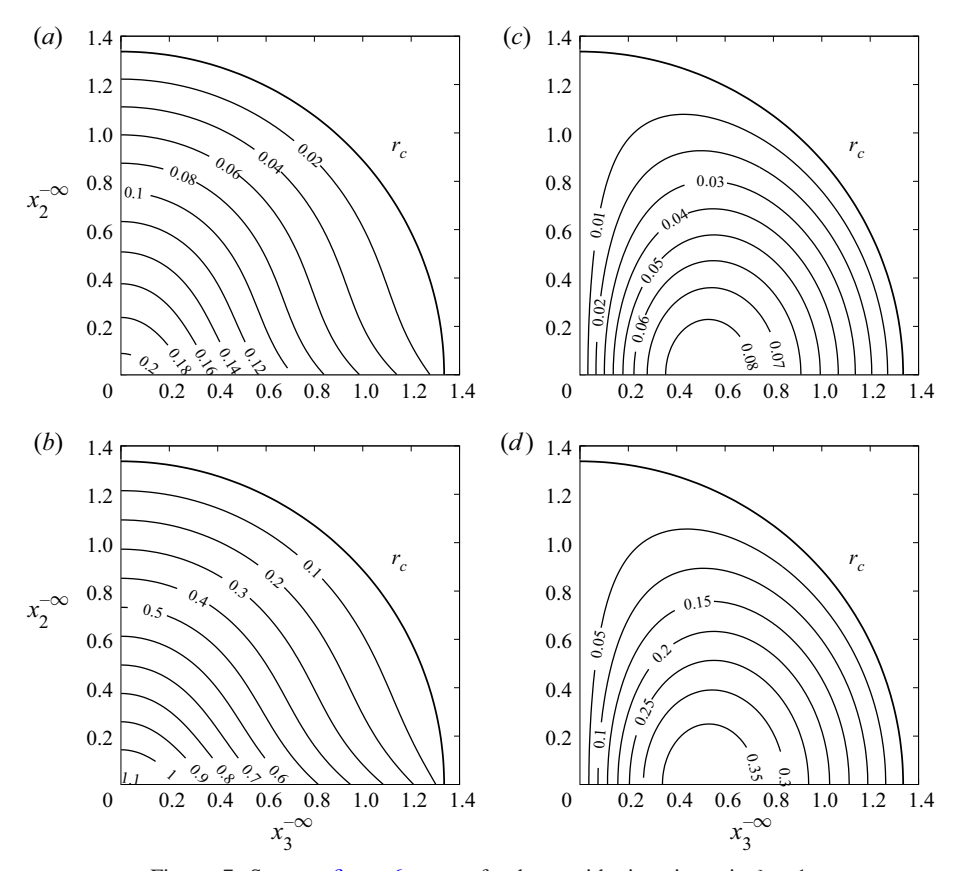


Figure 7. Same as figure 6, except for drops with viscosity ratio $\lambda = 1$.

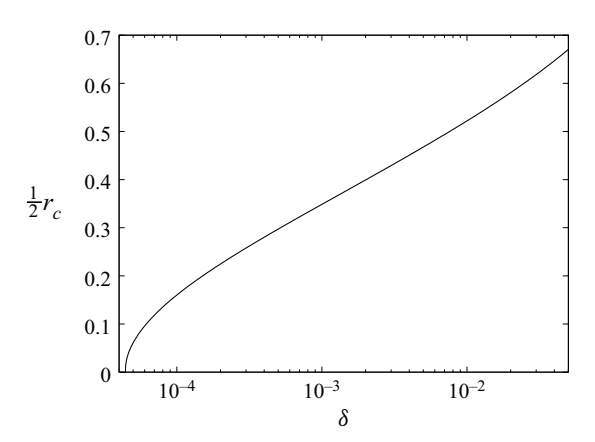


Figure 8. Collision cross-section for equal-size particles with roughness $\delta = d/a$ normalized by particle radius.

for particles of types i and j that undergo contact interactions. Our calculations support this relation but our results do not rely on it. The relation is used here to discuss the width of the boundary layer, X_c , that forms where the shear rate vanishes.

R.B. Reboucas, A.Z. Zinchenko and M. Loewenberg

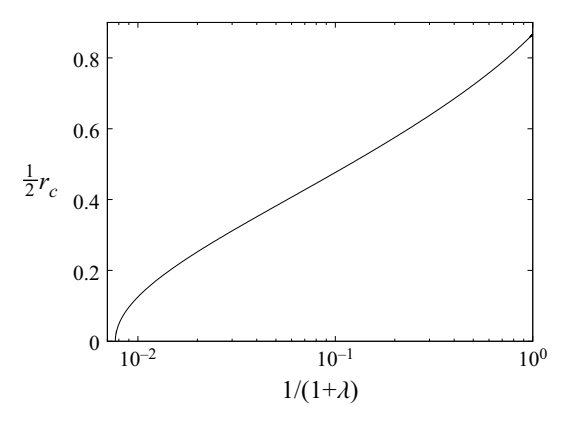


Figure 9. Same as figure 8, except for drops with viscosity ratio λ .

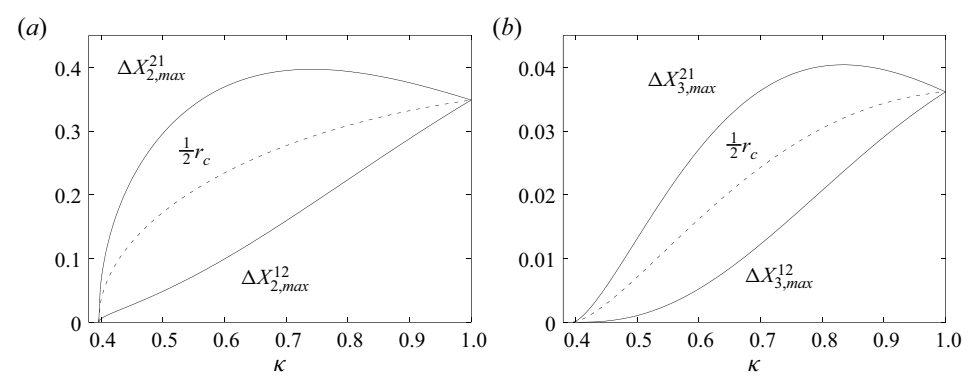


Figure 10. Maximum particle displacement magnitudes (solid lines) for rough particles, $\delta_1 = d/a_1 = 10^{-3}$, vs size ratio, $\kappa = a_2/a_1$, (a) in the velocity-gradient direction, and (b) in the vorticity direction; average of maximum displacement magnitudes (dashed lines); particle displacements and collision cross-section non-dimensionalized by radius of larger particle a_1 .

In a monodisperse suspension, maximum particle displacements are set by the collision cross-section, according to (4.3a,b), and $r_c = r_c^{ii}$, thus the boundary-layer thickness (4.6) reduces to

$$X_c^{ii} = \frac{1}{2}r_c^{ii}. (4.7)$$

The formula for the collision cross-section is provided in Appendix C. Below the critical values of particle roughness or permeability or above a critical value of the drop viscosity ratio, $r_c = 0$, as seen in figures 8 and 9; particle structuring is not predicted in this case. In a bidisperse suspension we have,

$$X_c = \max(\Delta_{2,max}^{21}, \frac{1}{2}r_{c,max}), \tag{4.8}$$

given that $\Delta X_2^{21} \geq \Delta X_2^{12}$, according to (4.4*a*–*c*). Here, $r_{c,max}$ is the maximum collision cross-section among the permutations of pairs of type-*i* and *j* particles, i.e. $r_{c,max} = max(r_c^{ii}, r_c^{ij}, r_c^{ij})$. In binary mixtures of particles that differ only in size, the collision cross-section between the larger particles usually controls $r_{c,max}$. Consider the case where larger particles are type-*i* and smaller, type *j*, particles differs only in size and $\kappa < 1$. In this case, we have $r_c^{ii} > r_c^{ij}$ because collision cross-sections increase monotonically with

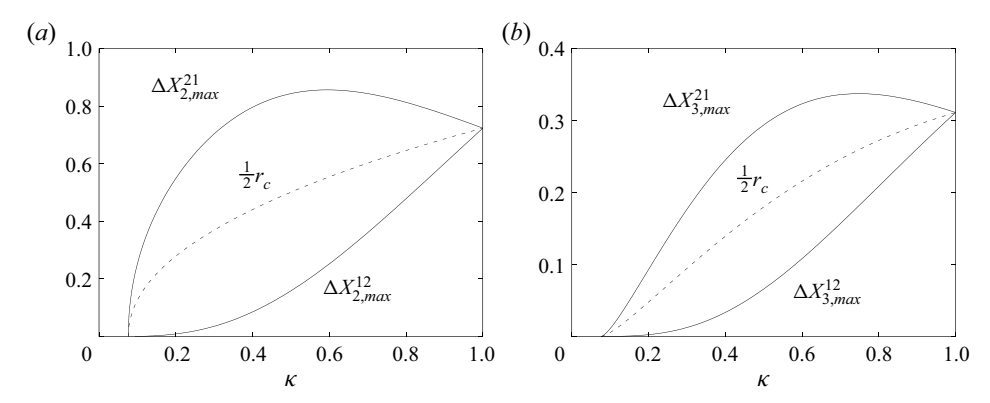


Figure 11. Same as figure 10, except for drops with viscosity ratio $\lambda = 1$.

size ratio, and usually $r_c^{ii} > r_c^{jj}$, because collision cross-sections scale with particle size. Accordingly, we have $r_{c,max} = r_c^{ii}$. For drops, $r_c^{ii} = \kappa^{-1} r_c^{jj}$ but this relation is inexact for rough and permeable particles because collision cross-sections increase monotonically with the size-dependent parameters, d/a and k/a^2 . Away from critical values of these parameters, however, the dependence is sub-linear, as seen in figure 8, thus $r_c^{ii} > r_c^{ij}$ holds and the relation $r_{c,max} = r_c^{ii}$ is retained.

The results shown in figures 10 and 11 illustrate relation (4.8), indicating that the boundary-layer thickness is controlled by heterogeneous pair interactions (i.e. $\Delta_{2,max}^{21} > r_{c,max}$) for moderate size ratios, and by the collision cross-section of the larger particles closer to the critical size ratio, κ^* . For $\kappa < \kappa^*$, displacements due to interactions between particles of different sizes vanish identically; in this case, the superposition approximation, described in § 3.2.3, holds exactly.

For particles with contact interactions, pair displacements and the resulting boundary-layer thickness scale with the size of the suspended particles. The particle distributions described in § 3.2 thus depend on particle size.

5. Particle distributions in Poiseuille flow: particles with contact interactions

Stationary particle distributions are presented here for suspensions in planar Poiseuille flow (2.32) with particles that undergo contact interactions using the analysis developed in § 4. The results here are specific examples of the results presented in § 3 for the case of rough particles and emulsion drops; permeable particles are also included through the established relation (4.1). The predictions for rough particles are compared with experimental measurements. No adjustable parameters are used for this comparison, aside from particle roughness; a nominal 1% roughness is used in all cases.

Transport coefficients (3.10*a,b*) were obtained by numerical evaluation of integrals (2.44)–(2.46) with particle displacements, ΔX_2^{ij} , obtained from quadratures of mobility functions, as described in § C.3. Stationary particle distributions in monodisperse suspensions were then obtained by evaluating formula (3.24). Stationary particle distributions in bidisperse mixtures were obtained by numerical integration of (3.9) using boundary conditions (3.18) appropriate for wide channels; approximate distributions were obtained by the superposition approximation (3.29). Results for monodisperse and bidisperse suspensions are presented in §§ 5.1 and 5.2, respectively. The limitation to dilute

suspensions is discussed in § 5.3 and a practical upper bound on the volume fraction is proposed.

In addition to diluteness, experiments for comparison require small particle Reynolds numbers and large Péclet numbers,

$$Re = \frac{\rho v_0 a^2}{\mu H} \ll 1, \quad Pe = \frac{v_0 a^3}{\mathcal{D}H^2} \gg 1,$$
 (5.1*a,b*)

where ρ and μ are the density and viscosity of the suspending phase fluid, \mathcal{D} is the Stokes-Einstein diffusivity, v_0 is the magnitude of the centreline velocity and H is the half-width of the channel. The Reynolds number is based on the characteristic shear rate, v_0/H , and the Péclet number is defined by criterion (2.33). For all experimental comparisons in this paper, $Re < 10^{-3}$ and $Pe > 10^{7}$. In bidisperse suspensions, these bounds apply with Reynolds number based on the larger particle and Péclet number based on the smaller. The assumptions of non-Brownian particles and creeping flow conditions are thus easily justified.

Another important consideration is the entry length L_{ss} required for particles to achieve a stationary distribution. An estimate for this quantity is given by $L_{ss} \sim v_0 t_{ss}$, where t_{ss} is the corresponding time scale for cross-flow particle transport. The latter scales as $t_{ss} \sim H^2/D$, where $D = O(\dot{\gamma} n_\infty X_c^5)$ is an estimate for the magnitude of the hydrodynamic diffusion coefficient of the particle. Then taking $\dot{\gamma} \sim v_0/H$ and $X_c = O(a)$, yields the desired estimate for the entry length based on the dilute theory

$$\left(\frac{L}{H}\right)_{ss} = \frac{1}{12\phi_{\infty}} \left(\frac{H}{a}\right)^2,\tag{5.2}$$

where the factor of 12 is included for consistency with Nott & Brady (1994). Accordingly, this estimate is the same as theirs except for the explicit first-order dependence on volume fraction. In a dilute polydisperse suspension, particles of different sizes a_i may require different entry lengths L_i to establish a stationary distribution, consistent with the superposition approximation. Thus, we introduce the generalization

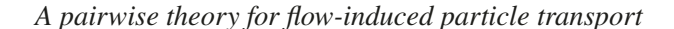
$$\left(\frac{L_i}{H}\right)_{ss} = \frac{1}{12\phi_{i\infty}} \left(\frac{H}{a_i}\right)^2. \tag{5.3}$$

Entry lengths L_{exp} used in experiments to test the predicted stationary distributions must satisfy

$$L_{exp}/L_{i_{xx}} > 1, (5.4)$$

where the index i is omitted for monodisperse suspensions. This criterion is satisfied for most of the experimental comparisons presented below, but as noted below, there are exceptions. The value of L_{exp}/L_{iss} is reported in the figure captions with experimental comparisons.

Dimensionless variables are used in this section with characteristic length set by the boundary-layer thickness X_c , the boundary layer thicknesses of individual species X_c^{ii} (related to the collision cross-section by (4.7)), or the channel width H, as indicated. The normalized number density \bar{N}_i , defined by (3.8b), is used for presenting theoretical predictions (i.e. the number density of each particle species normalized by its density at edge of the boundary layer).



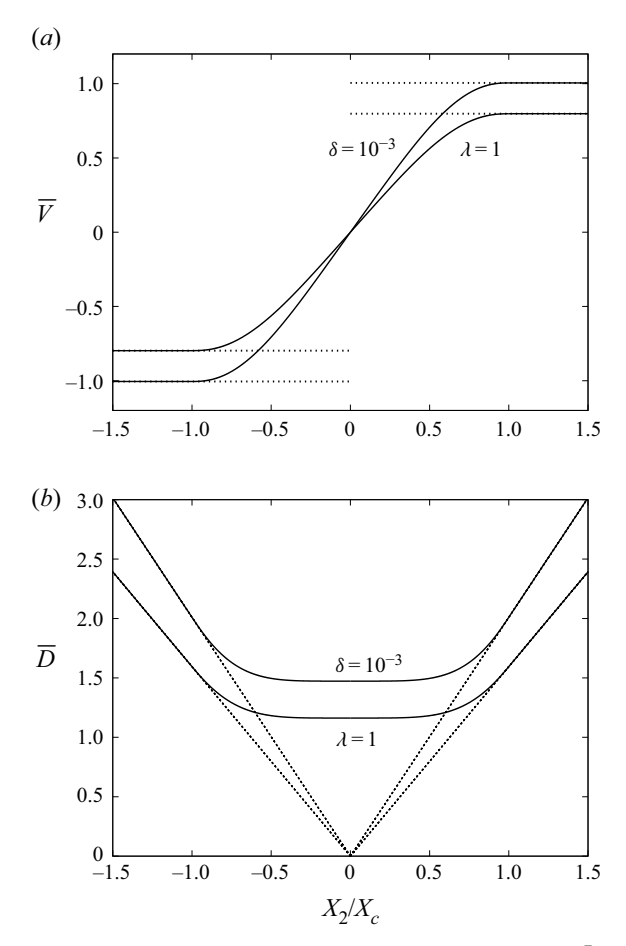


Figure 12. Dimensionless drift velocity (a) and diffusive (b) transport coefficients $\bar{D} = DX_c^{-6}$ and $\bar{V} = VX_c^{-5}$ (3.23a,b) for monodisperse suspensions of particles with roughness $\delta = d/a$ and drops with viscosity ratio λ , as indicated (solid lines); outer forms of transport coefficients (3.25a,b) (dotted lines). Boundary-layer thicknesses $X_c/a = 0.349$ for rough particles, and $X_c/a = 0.778$ for drops.

5.1. Particle distribution in monodisperse suspensions

Results for monodisperse suspensions are presented here, including particle distributions, the average deficit of particle density in the boundary layer compared with the singular outer distribution and the underlying diffusive and drift velocity transport coefficients. Predicted particle distributions are compared with predictions of the diffusive flux model (Phillips *et al.* 1992) and the experiments of Koh *et al.* (1994).

The results in figure 12 show that the drift velocity V but not the diffusion coefficient D vanishes at the centre of the channel, where the shear rate vanishes, and illustrate the respective odd and even symmetries of these quantities and their behaviour for $X_2 \rightarrow 0$, as discussed in § 2.3.3. These are the essential features that avoid the classical singularity at points of vanishing shear rate predicted by (2.37) and instead yield the smooth, non-singular behaviour predicted by (2.55). The dashed lines in figure 12 depict the local form of the transport coefficients that apply for $X_2 > X_c$. The anticipated second-derivative discontinuity in the transport coefficients at $X_2 = X_c$, discussed in § 2.3.3, is evident.

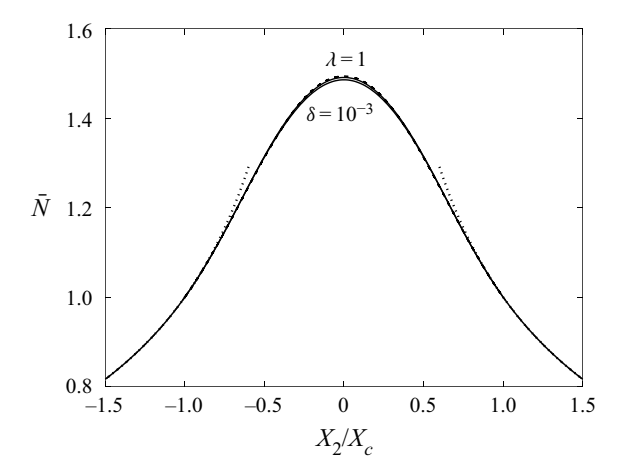


Figure 13. Distribution (3.24) for monodisperse suspension of particles with roughness $\delta = d/a$ and drops with viscosity ratio, λ , as indicated (solid lines); fit using (5.5) with $\Delta \bar{N} = 0.71$ (dashed line); outer solution (3.12) (dotted lines).

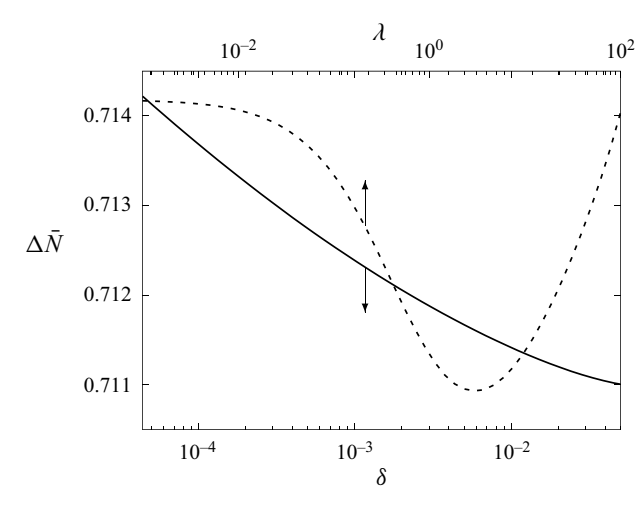


Figure 14. Average deficit of particle density in the boundary layer (3.27) for monodisperse suspensions of particles with roughness $\delta = d/a$ (solid line) and drops with viscosity ratio λ (dashed line).

Examples of particle distributions for rough particles and emulsion drops are shown in figure 13; the two distributions are barely distinguishable. Similar results were obtained for other values of roughness and viscosity ratios. The average deficit of particle density in the boundary layer is insensitive to the particle parameters (roughness and viscosity ratio) and has an almost constant value, $0.711 \le \Delta \bar{N} \le 0.714$, over a wide range of parameters, as seen in figure 14. The boundary-layer thickness (4.7) depends on details of the contact interactions between particles, as shown in figures 8 and 9; however, the particle distributions are almost independent of these details when displayed using the rescaled coordinate, X_2/X_c .

The above observation motivates a polynomial fit of the exact calculations. Enforcing continuity up to second derivatives at $y = \pm 1$, consistent with the expected continuity, discussed below (3.25*a*,*b*), and a prescribed value of the particle density deficit $\Delta \bar{N}$ yields

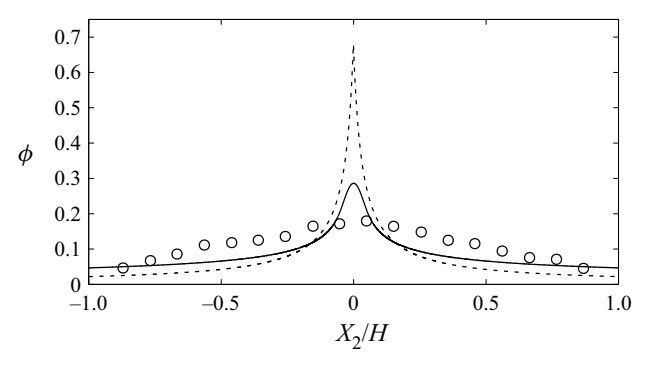


Figure 15. Particle distribution in monodisperse suspension with roughness $\delta = d/a = 10^{-2}$, bulk volume fraction $\phi_{\infty} = 10\%$ and channel width H/a = 8.8. Dilute theory (3.26) (solid line); classical diffusive flux model (5.6) (dashed line); data from Koh *et al.* (1994), $L_{exp}/L_{ss} = 5.0$ (\bigcirc).

$$\bar{N} \doteq \begin{cases} 1 + t + \frac{5}{2}t^2 + 35(3 - 4\Delta\bar{N})t^3 & |\tilde{y}| < 1\\ |\tilde{y}|^{-1/2} & |\tilde{y}| > 1 \end{cases} , \tag{5.5}$$

where $t = \frac{1}{4}(1 - \tilde{y}^2)$ and $\tilde{y} = X_2/H$. Inserting the value of $\Delta \bar{N}$ from figure 14 yields an approximation for \bar{N} with 0.2% maximum pointwise relative error; using the nominal value, $\Delta \bar{N} \doteq 0.71$, yields an approximation error of less than 1% for most values of roughness or viscosity ratio. Given its accuracy, the polynomial fit is appropriate for use with the (less accurate) superposition approximation.

An outline of the diffusive flux model is provided in Appendix B. For the purpose of comparing the dilute theory with the diffusive flux model (Phillips *et al.* 1992), we employ its frequently used approximate solution (Koh *et al.* 1994)

$$\phi = \frac{\phi_m}{1 + \alpha(X_2/H)},\tag{5.6}$$

where ϕ_m is the maximum packing fraction at the centreline of the channel, herein taken as $\phi_m = 0.68$ following Koh *et al.* (1994), and α is a numerical coefficient adjusted to enforce the bulk particle concentration (3.13). The prediction $\phi = \phi_m$ at the centreline is a consequence of using a suspension viscosity model as explained in Appendix B but is inappropriate for dilute suspensions. Moreover, the cusp-shape profile is unphysical and the corresponding absence of a particle scale is at odds with experiments (Koh *et al.* 1994).

The results in figures 15–17 show that the dilute theory is in approximate agreement with experiments for dilute suspensions and avoids the centreline cusp characteristic of the diffusive flux model. Empirical support for the predicted volume fraction and particle size dependence of the dilute theory is discussed in § 5.3.

5.2. Particle distribution in bidisperse suspensions

Results for bidisperse suspensions are presented here, including particle distributions, obtained by exact calculation and by superposition, and a parametric exploration of polydisperse enrichment due to the interactions between particles of different sizes. Predicted particle distributions are compared with the experiments of Lyon & Leal (1998b) in bidisperse suspensions.

R.B. Reboucas, A.Z. Zinchenko and M. Loewenberg

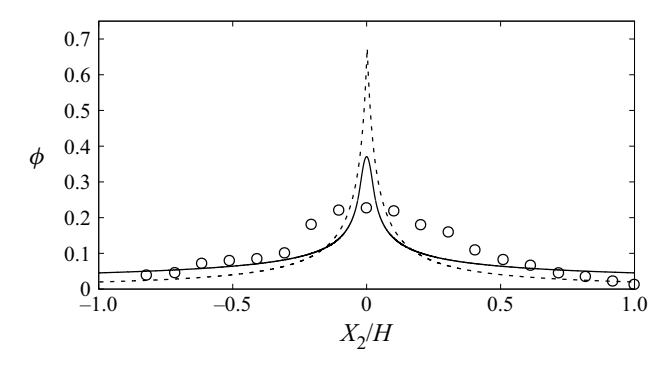


Figure 16. Same as figure 15 except H/a = 15.6; data (Koh et al. 1994) $L_{exp}/L_{ss} = 1.6$ (\bigcirc).

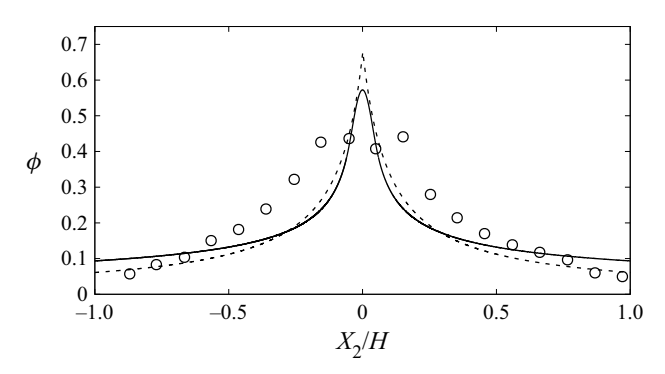


Figure 17. Same as figure 15 except $\phi_{\infty} = 20\%$; data (Koh et al. 1994) $L_{exp}/L_{ss} = 10$. (\bigcirc).

The bidisperse particle distributions shown in figure 18 show that small particles are enriched relative to large particles at the centreline, consistent with the approximately inverse square-root size dependence of the centreline density, discussed below (3.32). When rescaled using superposition variables (3.30a) and (3.31a), the distributions for both particles approximately collapse onto a universal distribution given by (5.5), as seen in figure 19.

Polydisperse enrichment (3.33) is a measure of the effect of interactions between particles of different sizes, an effect ignored by the superposition approximation. According to the discussion in § 3.2.3 and the remark at the end of § 4.4, the superposition approximation is expected to apply in bidisperse suspensions for $\kappa \lesssim \kappa^*$ and for $\kappa \approx 1$, as confirmed by the results presented in figures 20 and 21 which show $\Delta \bar{N}_{ij} \rightarrow 0$ in these limits. Particle roughness δ_1 and viscosity ratio λ determine the collision cross-section and thus the critical size ratio κ^* below which contact interactions are not predicted.

The results in figures 20 and 21 demonstrate that the superposition approximation provides an estimate of the particle distribution for all size ratios (examples for intermediate size ratio are shown in figure 18). The weak coupling for all size ratios is likely due to the absence of coupling outside the boundary layer, as discussed in \S 3.2.3. For rough particles, the superposition approximation is accurate to within a few per cent for a broad range of parameters; larger errors occur for emulsion drops because the displacements resulting from collisions between unequal drops exceed those for unequal rough particles, as seen by comparing figures 10(a) and 11(a).

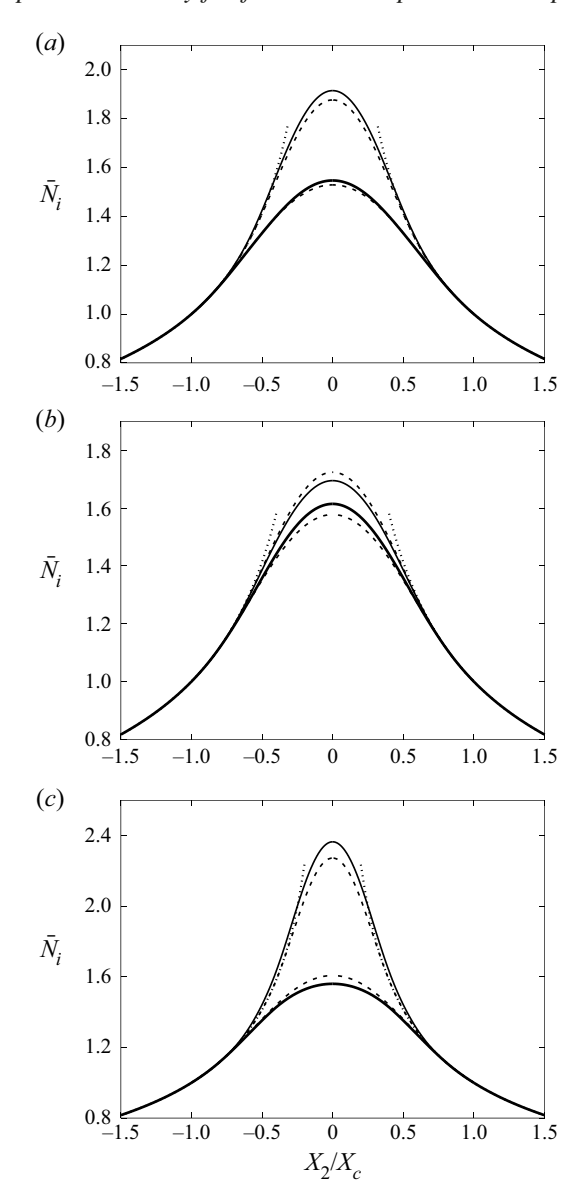


Figure 18. Particle distributions \bar{N}_i (i=1,2) in bidisperse suspensions with bulk volume fractions, $\phi_{1\infty} = \phi_{2\infty}$; rough particles $\delta_1 = d/a_1 = 10^{-3}$, size ratio $\kappa = a_2/a_1 = 0.6$ (a), $\kappa = 0.8$ (b); drops with viscosity ratio $\lambda = 1, \kappa = 1/2$ (c); numerical solution of (3.9) and (3.18) for large (thick solid line) and small (thin solid line) particles; superposition approximation (3.31a) (dashed lines), outer solution (3.12) (dotted lines).

Polydisperse enrichment in binary suspensions is most sensitive to size ratio. Polydisperse enrichment of larger particles is predicted for rough particles at all size ratios, as seen in panel (a) of figures 20 and 21, whereas smaller particles are enriched by the presence of much larger particles (small size ratios) and depleted by the presence of moderately larger particles. The particle distributions in panels (a) and (b) of figures 18 and 19 illustrate both regimes. By contrast, a polydisperse depletion of larger drops and enhancement of smaller drops is predicted for emulsions over most of the parameter range,

R.B. Reboucas, A.Z. Zinchenko and M. Loewenberg

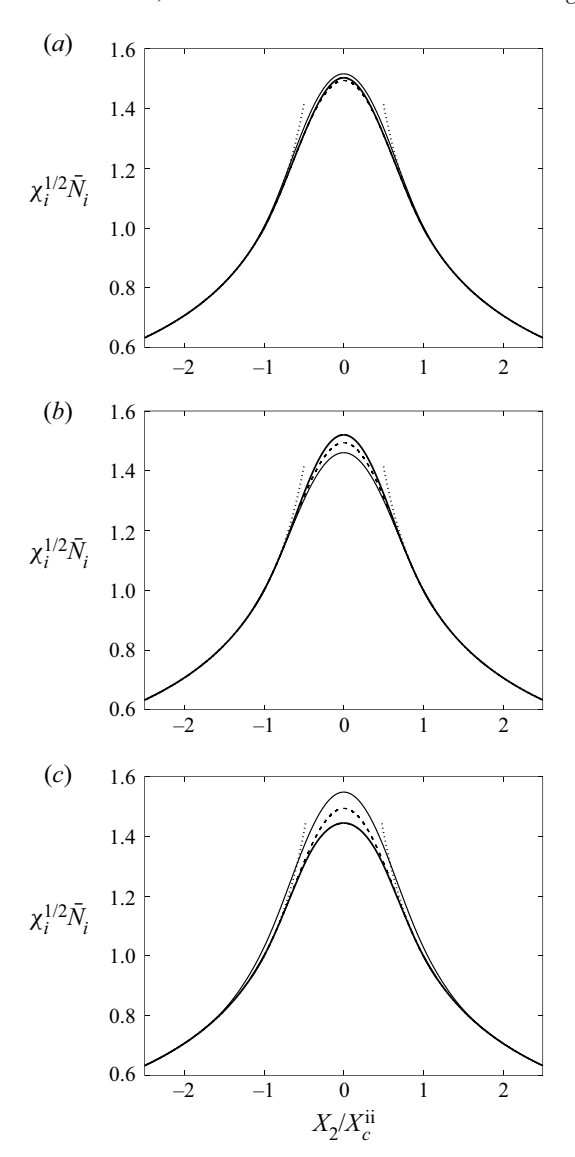


Figure 19. Same as figure 18 except rescaled using (3.30a) and (3.31a). Formula (3.24) (dashed lines).

as seen in panel (b) of figures 20 and 21. Panel (c) of figures 18 and 19 illustrates a typical drop distribution and shows the bigger effect of polydispersity.

The bulk composition, $\phi_{2\infty}/\phi_{1\infty}$, modulates the magnitude of polydisperse enrichment and depletion in suspensions of particles and drops but has less effect on whether it occurs, according to the results shown in figure 20. The viscosity ratio λ also modulates the magnitude of polydisperse enrichment and depletion as seen in figure 21(b). Particle roughness has a weaker effect on the magnitude of polydisperse enrichment and depletion; figure 21(a) shows that the polydisperse enrichment of large particles is insensitive to roughness.

Figures 22 and 23 show particle distributions in bidisperse suspensions with 30% volume fraction. The dilute theory quantitatively predicts the distribution of large particles

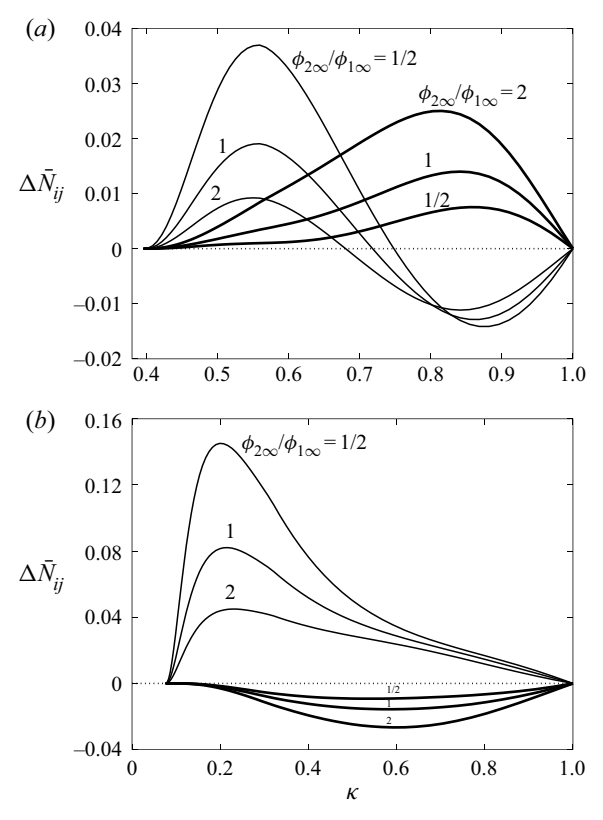


Figure 20. Polydisperse enrichment (3.33) for large (thick lines) and small (thin lines) particles, $\phi_{2\infty}/\phi_{1\infty}$ as indicated; (a) particles with roughness $\delta_1 = d/a_1 = 10^{-3}$, (b) drops with viscosity ratio $\lambda = 1$.

in the experiments of Lyon & Leal (1998b), except near the boundary, $|X_2|/H \ge 0.8$, where the data are reported to be unreliable (Lyon & Leal 1998b). Here, the superposition approximation of the dilute theory is used. Similarly, assuming independent transport of large particles, the authors fit their results for large particles using the suspension balance model for a monodisperse suspension (Morris & Brady 1998).

By contrast, the experiments depicted in figures 22 and 23 show essentially no flow-induced structuring of small particles; however, this is likely due to insufficient entry length to achieve the stationary distribution of small particles, as suggested by the authors (Lyon & Leal 1998b). As indicated in the figure captions, the entry length used in the experiments, L_{exp} , is at least 3.5 times shorter than the estimated length, L_{2ss} , required to establish a stationary distribution of the smaller particles. The slow evolution of particle microstructure is well known (Nott & Brady 1994; Phan-Thien & Fang 1996; Lyon & Leal 1998a); however, the hypothesis that particles of different sizes have distinct entry lengths has received less consideration (Semwogerere & Weeks 2008). The experiments reported by Lyon & Leal (1998b), including data not shown here, are consistent with distinct entry lengths predicted by (5.3).

There have been few studies that measure polydisperse enrichment, i.e. deviations from superposition resulting from hydrodynamic interactions between particles of different size. Semwogerere & Weeks (2008) observed polydisperse enrichment of large or small particles at the centreline and suggested that particles with a shorter entry length become

R.B. Reboucas, A.Z. Zinchenko and M. Loewenberg

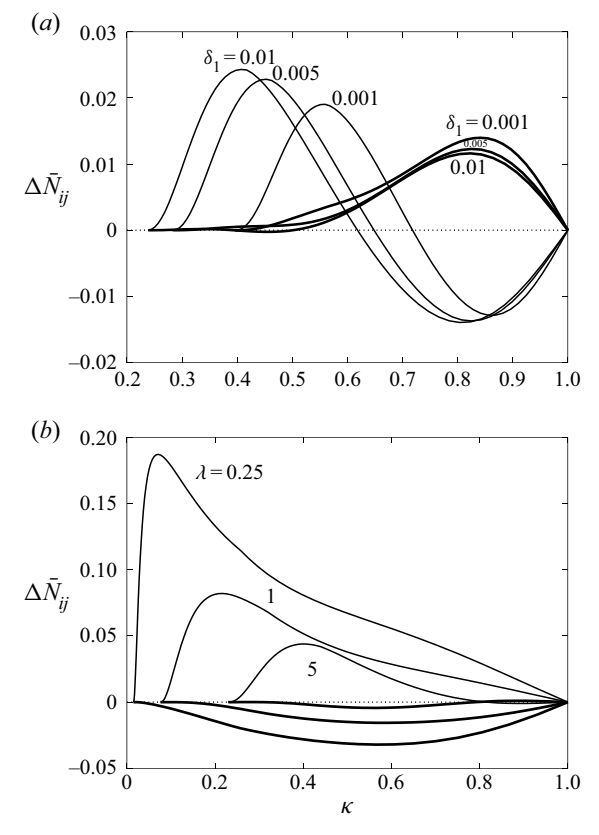


Figure 21. Polydisperse enrichment (3.33) for large (thick lines) and small (thin lines) particles, $\phi_{2\infty}/\phi_{1\infty} = 1$; (a) particles, roughness $\delta_1 = d/a_1$ as indicated; (b) drops, λ as indicated.

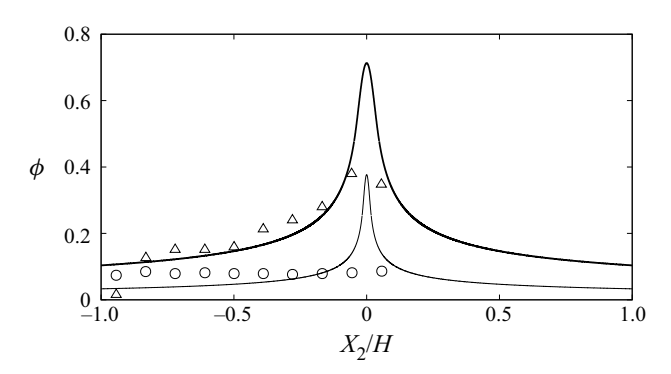


Figure 22. Particle distribution in bidisperse suspension with size ratio, $\kappa = a_2/a_1 = 0.3$, roughness $\delta_1 = d/a_1 = 10^{-2}$, bulk volume fractions $\phi_1 = 22.5\%$ and $\phi_2 = 7.5\%$, channel width $H/a_1 = 11$; dilute theory with superposition approximation (3.29) for large (thick line) and small (thin line) particles; data from Lyon & Leal (1998b) large (Δ) and small (Ω) particles, $L_{exp}/L_{1_{ss}} = 5.0$, $L_{exp}/L_{2_{ss}} = 0.14$.

more enriched in the centre region. Their results are less relevant here because colloidal (Brownian) particles were used in their study.

The experiments shown in figures 22 and 23 have been compared with a bidisperse diffusive flux model (Shauly et al. 1998; Chun et al. 2019). In planar Poiseuille flow, the

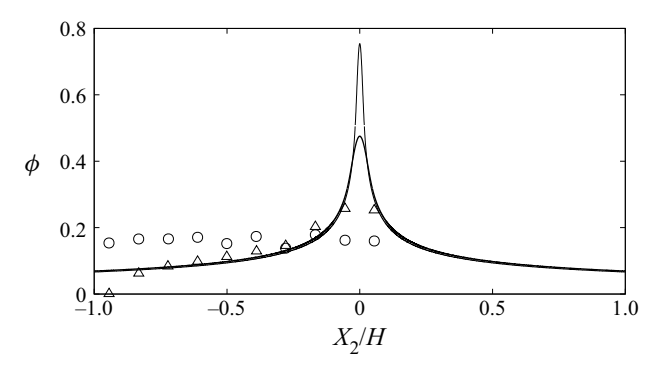


Figure 23. Same as figure 22, except for $\phi_1 = \phi_2 = 15$ %; data (Lyon & Leal 1998b) large (\triangle) and small (\bigcirc) particles, $L_{exp}/L_{1_{ss}} = 3.3$, $L_{exp}/L_{2_{ss}} = 0.28$.

bidisperse diffusive flux model predicts cusp-shaped distributions of both particle species: an upward cusp for the larger particles with a prescribed maximum volume fraction at the centreline, and a downward cusp for smaller particles with zero concentration at the centreline. By adjusting the physical parameters (size ratio, volume fractions and channel width), it was shown that the distribution of large particles could be made to fit the data but the predictions for the small particles were found to be qualitatively at odds with observations (Lyon & Leal 1998b; Chun et al. 2019).

5.3. Limitation of dilute theory

Here, we propose a volume fraction criterion for application of the dilute theory. Data aggregated from several experiments that satisfy this criterion and the required entry length (5.4) are used to further validate the dilute theory.

At larger volume fractions, the dilute theory fails by predicting a centreline volume fraction above the maximum packing limit. This observation provides a rough practical upper bound of the bulk particle volume fraction ϕ_{∞}^* in a monodisperse suspension and an upper bound $\phi_{i\infty}^*$ for each particle species in a polydisperse suspension. Using the superposition approximation (3.29) with polynomial fit (5.5), and setting the centreline particle volume fraction equal to the maximum packing limit, $\phi(0) = \phi_m$, we obtain

$$\phi_{i\infty}^*/\phi_m \approx 1.61\epsilon_i^{1/2},$$
 (5.7)

where ϵ_i is defined by (3.30*b*), and dropping the index *i* for monodisperse suspensions. For particles with 1% roughness, $X_c^{ii} \doteq 0.52a_i$, yielding the upper bound $\phi_{i\infty}^*/\phi_m \approx 1.16 \, (a_i/H)^{1/2}$. Taking $\phi_m = 0.68$, we find $\phi_\infty^* \approx 27 \, \%$ for the conditions described in figures 15 and 17, and $\phi_\infty^* \approx 20 \, \%$ for those in figure 16. For the conditions in figures 22 and 23, we have $\phi_{1\infty}^* \approx 24 \, \%$ and $\phi_{2\infty}^* \approx 13 \, \%$ but a smaller value may be warranted to accommodate a smaller value for ϕ_m .

All experiments from Koh *et al.* (1994) and Lyon & Leal (1998*a*) that satisfy constraint (5.7) and have the required entry length (5.4) are aggregated in figure 24, omitting data close to the wall, $|X_2|/H \ge 0.8$, as suggested by Lyon & Leal (1998*b*). According to (3.29), these data should collapse onto a single curve when re-plotted using

$$\bar{N}_{exp} = \frac{\phi_i/\phi_{i\infty}}{f(\epsilon_i)},\tag{5.8}$$

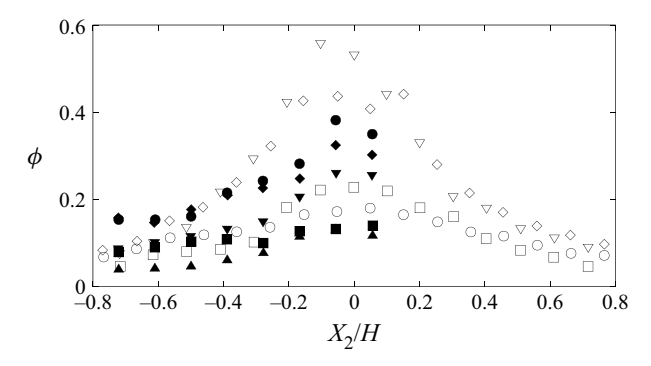


Figure 24. Data for monodisperse suspensions from Koh *et al.* (1994) $\phi = 10 \,\%$, H/a = 8.8, $L_{exp}/L_{ss} = 5.0$ (\bigcirc), H/a = 15.6, $L_{exp}/L_{ss} = 1.6$ (\square); $\phi = 20 \,\%$, H/a = 8.8, $L_{exp}/L_{ss} = 10$. (\lozenge), H/a = 15.6, $L_{exp}/L_{ss} = 3.2$ (\triangledown). Data for large particles in bidisperse suspensions from Lyon & Leal (1998*b*) $H/a_1 = 11$, $\phi_1 = 7.5 \,\%$, $L_{exp}/L_{1_{ss}} = 1.7$ (\blacktriangle), $\phi_1 = 10 \,\%$, $L_{exp}/L_{1_{ss}} = 2.2$ (\blacksquare), $\phi_1 = 15 \,\%$, $L_{exp}/L_{1_{ss}} = 3.3$ (\blacktriangledown), $\phi_1 = 20 \,\%$, $L_{exp}/L_{1_{ss}} = 4.4$ (\spadesuit), $\phi_1 = 22.5 \,\%$, $L_{exp}/L_{1_{ss}} = 5$ (\bullet).

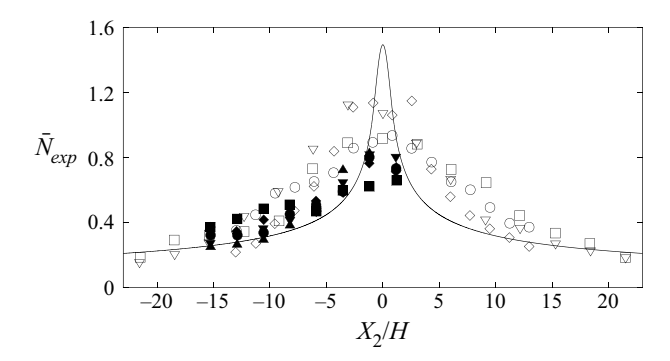


Figure 25. Data from figure 24 rescaled using (5.8); theoretical curve \bar{N} given by (3.24) (solid line).

where ϵ_i is given by (3.30b) and f(x) is defined by (3.28) with $\Delta \bar{N} \doteq 0.71$. The index i is dropped for monodisperse suspensions. As shown in figure 25, the data approximately collapse according to the dilute theory (and superposition approximation for bidisperse systems) when re-plotted this way.

The collapse of data for large particles in bidisperse suspensions (filled symbols) demonstrates the proportionality to bulk volume fraction because these data differ only in volume fraction. This is also seen in the collapse of data for monodisperse suspensions with 10% and 20% volume fractions with the same size particles (compare data points \bigcirc with \lozenge and \square with \triangledown). Validation for the size dependence predicted by the dilute theory is seen by comparing data for suspensions with different sized particles at fixed volume fractions (compare \bigcirc with \square and \lozenge with \triangledown).

Although the data are seen to collapse when re-plotted according to (5.8) in figure 25, the shape of the universal curve (solid line) is not accurately obtained. We note that the data for large particles from Lyon & Leal (1998b) (filled symbols) appear to attain the shape of the universal curve more closely than the data from Koh *et al.* (1994) (open symbols), consistent with the closer, quantitative agreement seen in figures 22 and 23 compared with that seen in figures 15–17. Systematic errors in the earlier study, discussed by Lyon & Leal (1998a), might account for this difference.

6. Conclusions

In this work we present a pairwise theory for particle distributions in dilute suspensions undergoing two-dimensional unidirectional flows, including planar Poiseuille and shear flows. There are no adjustable parameters.

A boundary layer is shown to form where the shear rate vanishes at the centre of Poiseuille flow; its thickness is set by the maximum of particle-related scales, including collision cross-sections, and net pairwise particle displacements. Size segregation occurs in the boundary layer leading to enrichment of smaller particles. Centreline particle densities scale approximately with the inverse square root of particle size. The finding of linearly vanishing drift velocities and non-vanishing diffusive fluxes in the boundary layer avoids the singular distribution predicted by other models. Outside of the boundary layer, particle distributions for each particle species are decoupled, independent of particle size, and obey a power law with exponent $-\beta/2$ in a power-law shear rate with exponent β . These results hold for systems with arbitrary symmetry-breaking pair interactions between particles.

Pair displacements for hydrodynamically interacting particles that undergo symmetry-breaking contact interactions were reduced to quadratures of mobility functions for spherical particles or drops. This result qualitatively advances the computational efficiency of calculations for particle distributions, making feasible an exploration of the three-dimensional parameter space that describes particle distributions in bidisperse suspensions, including size ratio, bulk composition and parameters that characterize particle interactions. Specific calculations were performed for rough particles and permeable particles (via an established equivalence relation) and for non-coalescing spherical drops.

After rescaling by the collision cross-section, particle distributions in monodisperse suspensions have an almost universal shape, nearly independent of particle roughness or drop viscosity. Polydisperse enrichment and depletion in bidisperse suspensions due to the coupling between particles of different sizes enhances the centreline concentration of large particles for the entire parameter space, whereas small particles are enriched for smaller size ratios and depleted for larger. By contrast, drops with mobile interfaces generally show polydisperse centreline enrichment of smaller drops and depletion of larger ones. Polydisperse enrichment is a comparatively weak effect, however, probably resulting from the absence of coupling between particle distributions outside the boundary layer. This allows particle distributions in polydisperse suspensions to be approximately described by a superposition of monodisperse distributions.

Within its limitations, the dilute theory is shown to be in agreement with available experiments for moderately dilute suspensions of non-Brownian particles. The predicted dependence on the bulk volume fraction and particle size are supported by these results. The experiments moreover support the superposition approximation. Some of the discrepancy between experiments and theory is likely the use of inadequate entry lengths. A transient analysis of particle distributions will help to confirm the theory. The superposition approximation may breakdown in smaller channels with significant size-dependent wall migration.

Funding. This work was supported by the National Science Foundation (grant number 1603806) and the Coordenaçõo de Aperfeiçoamento de Pessoal de Nível Superior - Brasil (Capes) (Finance Code 001).

Declaration of interests. The authors report no conflict of interest.

Author ORCIDs.

Rodrigo B. Reboucas https://orcid.org/0000-0001-8982-3553;

- Alexander Z. Zinchenko https://orcid.org/0000-0001-7925-6567;
- Michael Loewenberg https://orcid.org/0000-0003-1735-0755.

Appendix A. Derivation of transport coefficients in planar Poiseuille flows

In this section, we present a derivation of the transport coefficients in the velocity-gradient direction in regions where the shear rate vanishes. Inserting the exact relative particle velocity magnitude (2.34) into the particle flux integral (2.4), and transforming to the cylindrical coordinate system shown in figure 2, yields

$$F_{ij2}(X_2) = \dot{\gamma}_2' \int_0^{2\pi} \int_0^{r_c^{ij}} r^{-\infty} |\sin \theta| \left[\int_{-\Delta X_2^{ij}}^0 n_i (X_2^{i,-\infty}) n_j (X_2^{j,-\infty}) \right] dx_2 + X_2^{i,-\infty} + \frac{1}{2} r^{-\infty} \sin \theta dx_2^{i,-\infty} r^{-\infty} dr^{-\infty} d\theta.$$
(A1)

Here, $X_2^{i,-\infty}$ is the distance of particle-*i* from the plane X_2 where the flux is measured and $X_2^{i,-\infty}$ is the distance of particle-*j* from this plane, as depicted in figure 1.

We proceed by inserting linear variations in number density (2.13) into (A1) but the complete velocity field (2.34) is used here, not a linearized approximation, because the latter is inconsistent in the region where the shear rate vanishes. Splitting the angular θ -integration in (A1) into two ranges: $0 \le \theta < \pi$ and $\pi \le \theta < 2\pi$, and using the symmetry relation (2.7) to consolidate integration to the range $0 \le \theta < \pi$ yields

$$I_{ij}^{(1)}(X_{2}) = \frac{1}{2} \frac{1}{|X_{2}|} \int_{0}^{\pi} \int_{0}^{r_{c}^{ij}} r^{-\infty} \sin \theta \left[\int_{0}^{-\Delta X_{2}^{ij}} \left(\left| X_{2}^{i,-\infty} + \frac{1}{2} r^{-\infty} \sin \theta - X_{2} \right| \right. \right.$$

$$\left. + \left| X_{2}^{i,-\infty} + \frac{1}{2} r^{-\infty} \sin \theta + X_{2} \right| \right) X_{2}^{i,-\infty} dX_{2}^{i,-\infty} \right] r^{-\infty} dr^{-\infty} d\theta, \qquad (A2)$$

$$I_{ij}^{(2)}(X_{2}) = \frac{1}{2} \frac{1}{|X_{2}|} \int_{0}^{\pi} \int_{0}^{r_{c}^{ij}} r^{-\infty} \sin \theta \left[\int_{0}^{-\Delta X_{2}^{ij}} \left(\left| X_{2}^{i,-\infty} + \frac{1}{2} r^{-\infty} \sin \theta - X_{2} \right| \right.$$

$$\left. + \left| X_{2}^{i,-\infty} + \frac{1}{2} r^{-\infty} \sin \theta + X_{2} \right| \right)$$

$$\left. (r^{-\infty} \sin \theta + X_{2}^{i,-\infty}) dX_{2}^{i,-\infty} \right] r^{-\infty} dr^{-\infty} d\theta, \qquad (A3)$$

and

$$I_{ij}^{(3)}(X_2) = \frac{1}{2} \int_0^{\pi} \int_0^{r_c^{ij}} r^{-\infty} \sin \theta \left[\int_0^{-\Delta X_2^{ij}} \left(\left| X_2^{i,-\infty} + \frac{1}{2} r^{-\infty} \sin \theta - X_2 \right| - \left| X_2^{i,-\infty} + \frac{1}{2} r^{-\infty} \sin \theta + X_2 \right| \right) dX_2^{i,-\infty} \right] r^{-\infty} dr^{-\infty} d\theta,$$
 (A4)

where $-\Delta X_2^{ij} > 0$ according to (2.49).

Equations (A2)–(A4) indicate that integrals $I^{(1)}(X_2)$ and $I^{(2)}(X_2)$ are even functions and $I^{(3)}(X_2)$ is an odd function of X_2 . Accordingly, we can make the replacement $X_2 \to |X_2|$

in these equations without other changes, except multiplying (A4) by $\operatorname{sign}(X_2)$. After so doing, the absolute value can be removed from the second term in each integrand because its argument, $X_2^{i,-\infty} + \frac{1}{2}r^{-\infty}\sin\theta + |X_2|$, is intrinsically positive for $0 < \theta < \pi$. However, removing the absolute value of the first term of each integrand requires splitting the range of the $X_2^{i,-\infty}$ integration in two intervals,

$$0 < X_2^{i,-\infty} < -\Delta X_2^{ij} B(X_2'),$$
 (A5)

and

$$-\Delta X_2^{ij}B(X_2') < X_2^{i,-\infty} < -\Delta X_2^{ij}, \tag{A6}$$

where X_2' is defined by (2.47) and B(x) is the ramp function (2.48). After implementing the foregoing manoeuvres, integrals (A2)–(A4) become

$$I_{ij}^{(1)}(X_{2}) = \frac{1}{|X_{2}|} \int_{0}^{\pi} \int_{0}^{r_{c}^{ij}} r^{-\infty} \sin \theta \left[\int_{0}^{-\Delta X_{2}^{ij}B(X_{2}^{i})} |X_{2}| X_{2}^{i,-\infty} dX_{2}^{i,-\infty} dX_{2}^{i,-\infty} \right]$$

$$+ \int_{-\Delta X_{2}^{ij}B(X_{2}^{i})}^{-\Delta X_{2}^{ij}} \left(X_{2}^{i,-\infty} + \frac{1}{2} r^{-\infty} \sin \theta \right) X_{2}^{i,-\infty} dX_{2}^{i,-\infty} \right] r^{-\infty} dr^{-\infty} d\theta, \quad (A7)$$

$$I_{ij}^{(2)}(X_{2}) = \frac{1}{|X_{2}|} \int_{0}^{\pi} \int_{0}^{r_{c}^{ij}} r^{-\infty} \sin \theta \left[\int_{0}^{-\Delta X_{2}^{ij}B(X_{2}^{i})} |X_{2}| (X_{2}^{i,-\infty} + r^{-\infty} \sin \theta) dX_{2}^{i,-\infty} \right]$$

$$+ \int_{-\Delta X_{2}^{ij}B(X_{2}^{i})}^{-\Delta X_{2}^{ij}} \left(X_{2}^{i,-\infty} + \frac{1}{2} r^{-\infty} \sin \theta \right) (X_{2}^{i,-\infty} + r^{-\infty} \sin \theta) dX_{2}^{i,-\infty} \right]$$

$$+ \int_{-\Delta X_{2}^{ij}B(X_{2}^{i})}^{-\Delta X_{2}^{ij}B(X_{2}^{i})} |X_{2}| dX_{2}^{i,-\infty} \right] r^{-\infty} dr^{-\infty} d\theta. \quad (A8)$$

$$+ \int_{-\Delta X_{2}^{ij}B(X_{2}^{i})}^{-\Delta X_{2}^{ij}B(X_{2}^{i})} |X_{2}| dX_{2}^{i,-\infty} \right] r^{-\infty} dr^{-\infty} d\theta. \quad (A9)$$

In this form, the $X_2^{i,-\infty}$ integration can be performed to yield the desired result given by (2.44)–(2.46).

Appendix B. Diffusive flux model

For comparison purposes, a brief outline of the diffusive flux model (Phillips *et al.* 1992) is presented here, including a local analysis of the predicted behaviour at the centreline of the flow. From (11) in Phillips *et al.* (1992), the stationary particle distribution is governed by

$$K_c(\phi^2 \gamma' + \gamma \phi \phi') + K_{\eta}(\gamma [\log \eta(\phi)]' \phi^2) = 0, \tag{B1}$$

where K_c and K_{η} are dimensionless constants, γ is the shear rate non-dimensionalized by v_0/H , $\eta(\phi)$ is the particle-concentration-dependent viscosity of the suspension and primes

denote derivatives with respect to $\tilde{y} = X_2/H$. By a momentum balance, the shear rate is given by

$$\gamma = |\tilde{y}|/\eta(\phi). \tag{B2}$$

Krieger's empirical model (Krieger 1972) for the suspension viscosity is used to complete the description

$$\eta/\eta_0 = (1 - \phi/\phi_m)^{-\beta},$$
 (B3)

where η_0 is the viscosity of the continuous-phase liquid. Here, $\phi = \phi_m$ is the maximum packing fraction of the suspension, where the viscosity diverges, and $\beta \doteq 1.82$. Note that particle size does not enter the diffusive flux model.

The shear rate vanishes at the centreline but γ' does not. According to (B1), a non-singular particle distribution requires divergence of the viscosity, thus $\phi \to \phi_m$ is required at $\tilde{y} = 0$. The solution of (B1)–(B3) has a cusp at the centreline,

$$\phi/\phi_m = 1 - M_4 |\tilde{y}|^c + O(\tilde{y}^{2c}), \quad \tilde{y} \to 0,$$
 (B4)

where M_4 is a positive constant determined by the solution away from the centre and the exponent is given by

$$c = \frac{K_c}{K_n - K_c} \beta^{-1}.$$
 (B5)

Phillips *et al.* (1992) report $K_c/K_n \doteq 0.66$, thus $c \approx 1$.

An approximate solution of (B1)–(B3) for planar Poiseuille flow (Koh *et al.* 1994), consistent with the local analysis above, is given by (5.6).

Appendix C. Analytical integration of contacting pair trajectories

Analytical integration formulas are derived here for contacting particle trajectories, such as those shown in figures 4 and 5. As illustrated, widely separated particles with upstream offsets within the collision cross-section are brought together by the imposed flow, reach the contact surface (ii), move along the contact surface in the compressional quadrant of the flow (ii–iii), separate at the edge of the compressional quadrant (iii) and again become widely separated. A contact force prevents particle overlap on the contact surface portion of trajectories (ii–iii). The relative and pair motion of the particles are separately treated. The former has been previously analysed in classical works as cited below; integration of the pair motion is new. Both are needed to determine particle displacements.

C.1. Particle trajectories

In a linear flow under creeping flow conditions, the trajectories of non-Brownian, neutrally buoyant, inertialess particles with labels 1 and 2 are described by Batchelor & Green (1972b)

$$V_1 = V_1^{(\infty)} - [A_1(s)\hat{r}\hat{r} + B_1(s)(I - \hat{r}\hat{r})] \cdot E \cdot \hat{r}, \tag{C1}$$

and

$$V_2 = V_2^{(\infty)} - [A_2(s)\hat{r}\hat{r} + B_2(s)(I - \hat{r}\hat{r})] \cdot E \cdot \hat{r}, \tag{C2}$$

where, $r = X^{(2)} - X^{(1)}$ is the vector between the particle centres, as shown in figure 26, $\hat{r} = r/|r|$ is a unit vector along the line of centres, I is the identity tensor and $s = |r|/\bar{a}$ is the centre-to-centre separation normalized by the average radius. The undisturbed particle

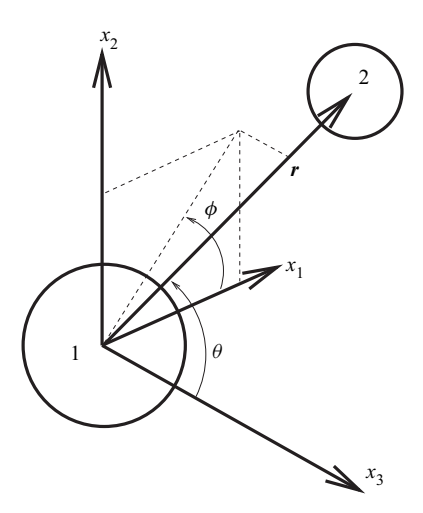


Figure 26. Spherical coordinate system (r, θ, ϕ) for pair trajectories, where $x_1 = r \sin \theta \cos \phi$, $x_2 = r \sin \theta \sin \phi$, $x_3 = r \cos \theta$.

velocities are $V_i^{(\infty)} = E \cdot X^{(i)} + \omega \times X^{(i)}$ (i = 1, 2), where E is the rate of strain, and ω is the angular velocity. In simple shear flow

$$E = \dot{\gamma} \begin{pmatrix} 0 & 1/2 & 0 \\ 1/2 & 0 & 0 \\ 0 & 0 & 0 \end{pmatrix}, \quad \omega = \dot{\gamma} (0, 0, -1/2), \tag{C3a,b}$$

where $\dot{\gamma}$ is the magnitude of the local shear rate. In (C1) and (C2), A_i and B_i (i=1,2), respectively, are mobility functions that incorporate the effect of hydrodynamic interactions on the particle velocities parallel and normal to the line of centres of the pair. Mobility functions depend also on the particle size ratio $\kappa = a_2/a_1$, and for spherical drops, also on the drop-to-continuous-phase viscosity ratio, λ .

C.2. Trajectory integration

The relative motion of the particles are described by the trajectory equations (Batchelor & Green 1972b)

$$\frac{\mathrm{d}s}{\mathrm{d}t} = (1 - A)s\sin^2\theta\sin\phi\cos\phi,\tag{C4}$$

$$\frac{\mathrm{d}\theta}{\mathrm{d}t} = (1 - B)\sin\theta\cos\theta\sin\phi\cos\phi,\tag{C5}$$

$$\frac{d\phi}{dt} = -\frac{1}{2} + \frac{1}{2}(1 - B)\cos 2\phi,\tag{C6}$$

where the spherical coordinates defined in figure 26 are used. The pair motion of the particles is described by

$$\frac{\mathrm{d}\bar{x}_1}{\mathrm{d}t} = \bar{x}_2 - \left[\frac{B_p x_2}{2} + (A_p - B_p) \frac{x_1^2 x_2}{s^2} \right],\tag{C7}$$

$$\frac{\mathrm{d}\bar{x}_2}{\mathrm{d}t} = -\left[\frac{B_p x_1}{2} + (A_p - B_p) \frac{x_1 x_2^2}{s^2}\right],\tag{C8}$$

$$\frac{d\bar{x}_3}{dt} = -(A_p - B_p) \frac{x_1 x_2 x_3}{s^2}.$$
 (C9)

Here, t is strain, and x and \bar{x} , respectively, are the relative and pair positions

$$x = X^{(2)} - X^{(1)}, \quad \bar{x} = X^{(1)} + X^{(2)}.$$
 (C10a,b)

Relative and pair mobilities are denoted $M = M_2 - M_1$ and $M_p = M_1 + M_2$, respectively, where M = A or B. In prior analyses, only the relative mobilities were required (Batchelor & Green 1972a,b; Zinchenko 1978, 1980, 1983; Wilson 2005). Here, pair mobilities are also required because the displacements of both particles, not just their relative displacement, are needed. By symmetry, we can restrict our attention to relative positions x in the positive quarter-plane. Accordingly, the initial positions are

$$x_1^{(i)} = -\infty, \quad x_2^{(i)}, \ x_3^{(i)} \ge 0,$$
 (C11*a,b*)

but $\bar{x}^{(i)}$ is arbitrary because only differences of the pair position are significant.

Integrating equations (C4)–(C6) with initial conditions (C11a) yields (Batchelor & Green 1972b; Zinchenko 1983)

$$x_2(s) = \varphi(s)[(x_2^{\infty})^2 + \Psi(s)]^{1/2},$$
 (C12)

$$x_3(s) = x_3^{\infty} \varphi(s), \tag{C13}$$

$$x_1(s) = \mp \sqrt{s^2 - x_2^2 - x_3^2},$$
 (C14)

where x_2^{∞} and x_3^{∞} are the cross-flow coordinates of the far-field relative position of the particles at $s \to \infty$. The functions $\varphi(s)$ and $\Psi(s)$ are given by

$$\varphi(s) = \exp\left[\int_{s}^{\infty} \frac{A(s') - B(s')}{1 - A(s')} \frac{\mathrm{d}s'}{s'}\right],\tag{C15}$$

and

$$\Psi(s) = \int_{s}^{\infty} \frac{B(s')s'}{[1 - A(s')]\varphi^{2}(s')} ds'.$$
 (C16)

The minus sign applies in (C14) for $\pi/2 < \phi < \pi$; the + sign applies for $0 < \phi < \pi/2$. Dividing equations (C8) and (C9) by (C4) and integrating yields the pair positions

$$\bar{x}_2(s) = \bar{x}_2^{\infty} + \bar{\Psi}(s, x_2^{\infty}),$$
 (C17)

and

$$\bar{x}_3(s) = \bar{x}_3^{\infty} + \overline{\varphi}(s, x_3^{\infty}), \tag{C18}$$

where \bar{x}_2^{∞} and \bar{x}_3^{∞} are the corresponding coordinates of the far-field pair position. The functions $\overline{\varphi}(s, x_3^{\infty})$ and $\bar{\Psi}(s, x_2^{\infty})$ are defined

$$\bar{\varphi}(s, x_3^{\infty}) = \int_s^{\infty} \frac{[A_p(s') - B_p(s')]x_3(s', x_3^{\infty})}{[1 - A(s')]s'} \, \mathrm{d}s', \tag{C19}$$

and

$$\bar{\Psi}(s, x_2^{\infty}) = \int_s^{\infty} \left[\frac{B_p(s')s'}{2[1 - A(s')]x_2(s', x_2^{\infty})} + \frac{[A_p(s') - B_p(s')]x_2(s', x_2^{\infty})}{[1 - A(s')]s'} \right] ds', \quad (C20)$$

where $x_2(s, x_2^{\infty})$ and $x_3(s, x_3^{\infty})$ are defined by (C12) and (C13). The streamwise coordinate of the pair position, \bar{x}_1 , does not affect the cross-flow particle distribution.

C.2.1. Trajectories on contact surface

The contact surface is defined by $s = s^*$, where $s^* = 2$ for permeable particles and drops and $s^* = 2 + \bar{\delta}$ for particles with surface roughness. In the compressional quadrant of the flow, the relative trajectory on the contact surface is described by setting the relative radial velocity to zero; particles separate in the extensional quadrant. The polar and azimuthal angles (θ, ϕ) evolve according to (C5) and (C6) over the range

$$\frac{\pi}{2} \le \phi \le \phi_0,\tag{C21}$$

where (θ_0, ϕ_0) is the initial point of contact (point (ii) in figures 4 and 5); separation occurs at $\phi = \pi/2$ (point (iii)). Dividing the two equations and integrating yields (Rother & Davis 2001)

$$\theta_1(\phi) = \tan^{-1} \left(\tan \theta_0 \sqrt{\frac{1 - B_1^* \cos(2\phi_0)}{1 - B_1^* \cos 2\phi}} \right),$$
 (C22)

where $B_1^* = 1 - B(s^*)$.

The pair motion on the contact surface is obtained by dividing (C8) and (C9) by (C6) and integrating the range (C21) to yield,

$$\bar{x}_2^*(\phi) = \bar{x}_2^*(\phi_0) + \Omega(\phi),$$
 (C23)

and

$$\bar{x}_3^*(\phi) = \bar{x}_3^*(\phi_0) + \chi(\phi),$$
 (C24)

where the functions $\Omega(\phi)$ and $\chi(\phi)$ are defined by

$$\Omega(\phi) = \int_{\phi_0}^{\phi} \frac{\left[\hat{r}_3^2(\phi') - 1\right] \left[B_p^* \hat{r}_1(\phi') + 2(A_p' - B_p^*) \hat{r}_1(\phi') \hat{r}_2^2(\phi')\right]}{\frac{1}{2} B^* \left[2 \hat{r}_2^2(\phi') + \hat{r}_3^2(\phi') - 1\right] - \hat{r}_2^2(\phi')} d\phi', \tag{C25}$$

and

$$\chi(\phi) = \int_{\phi_0}^{\phi} \frac{\left[\hat{r}_3^2(\phi') - 1\right]\left[2(A_p' - B_p^*)\hat{r}_1(\phi')\hat{r}_2(\phi')\hat{r}_3(\phi')\right]}{\frac{1}{2}B^*\left[2\hat{r}_2^2(\phi') + \hat{r}_3^2(\phi') - 1\right] - \hat{r}_2^2(\phi')} d\phi'.$$
 (C26)

Here, $\hat{r} = (\hat{r}_1, \hat{r}_2, \hat{r}_3)$ is the relative position vector on the contact surface

$$\hat{\mathbf{r}} = (\sin[\theta_1(\phi)]\cos\phi, \sin[\theta_1(\phi)]\sin\phi, \cos[\theta_1(\phi)]), \tag{C27}$$

where $\theta_1(\phi)$ is given by (C22). The mobility functions B_p^* and B^* in (C25) and (C26) are evaluated at $s = s^*$, except that contact friction for rough particles, enters through a modified value of B^* , as discussed in § C.4.

The quantity A'_p in (C25) and (C26) is the modified contact mobility that encompasses the correction resulting from the action of the contact force, F_c . The latter quantity is

required to prevent particle overlap and is determined by the force balance,

$$V_{12} \cdot \hat{r} = 2(1 - A^*)(E : \hat{r}\hat{r}) - \frac{F_c}{\mu \bar{a}^2 \dot{\gamma}} G^* = 0,$$
 (C28)

where μ is the continuous-phase viscosity, and G^* is the relative radial mobility function evaluated at contact. The contact force modifies the pair velocity for unequal size particles,

$$V_{12}^{p} \cdot \hat{\mathbf{r}} = -2A_{p}^{*}(E : \hat{\mathbf{r}}\hat{\mathbf{r}}) - \frac{F_{c}}{\mu \bar{a}^{2} \dot{\gamma}} G_{p}^{*},$$
 (C29)

where G_p^* is the pair radial mobility function evaluated at contact. Substituting the normal force derived from (C28) into (C29) yields

$$V_{12}^p \cdot \hat{r} = -2A_p'(E : \hat{r}\hat{r}), \tag{C30}$$

where $A_p' = A_p^* + (1 - A^*)G_p^*/G^*$ is the modified axisymmetric pair mobility that appears in formulas (C25) and (C26) (Zarraga & Leighton 2001). The modified mobility represents a higher-order correction, e.g. an $O(\bar{\delta})$ correction for rough particles and an $O(K^{2/5})$ correction for permeable particles. There is no contact force for non-coalescing spherical drops because $1 - A^* = 0$, according to the model described in § 4.1.3.

C.3. Net cross-flow displacements

The indefinite trajectory integrals derived in § C.2 are combined here to yield formulas for the net relative and pair displacements in terms of the pair mobility functions. Relative and pair trajectory segments, (i–ii), (ii–iii) and (iii–iv) are defined in figure 4.

From (C12) and (C13), the relative cross-flow position at the contact point is

$$x_2^{(ii)} = \varphi^* [(x_2^{(i)})^2 + \Psi^*]^{1/2}, \quad x_3^{(ii)} = \varphi^* x_3^{(i)},$$
 (C31*a,b*)

where φ^* and Ψ^* are the functions (C15) and (C16) evaluated on the contact surface, $s = s^*$, and $x^{(i)}$ is the initial condition (C11a,b). The polar and azimuthal angles at the initial contact point (θ_0, ϕ_0) , are given by

$$2\cos\theta_0 = x_3^{(ii)}, \quad 2\sin\theta_0\sin\phi_0 = x_2^{(ii)}.$$
 (C32a,b)

The separation point is given by

$$x_2^{\text{(iii)}} = 2\sin\left[\theta_1\left(\frac{\pi}{2}\right)\right] \quad x_3^{\text{(iii)}} = 2\cos\left[\theta_1\left(\frac{\pi}{2}\right)\right],\tag{C33a,b}$$

where $\theta_1(x)$ is the function (C22). The final relative position of the particles in the cross-flow plane is

$$x_2^{(\text{iv})} = \left[\left(\frac{x_2^{(\text{iii})}}{\varphi^*} \right)^2 - \Psi^* \right]^{1/2}, \quad x_3^{(\text{iv})} = \frac{x_3^{(\text{iii})}}{\varphi^*}.$$
 (C34*a,b*)

The displacement relations for the pair motion are obtained from (C17) and (C18) and (C23) and (C24), yielding the pair position

$$\bar{x}_2^{(ii)} = \bar{\Psi}^*(x_2^{(i)}), \quad \bar{x}_3^{(ii)} = \bar{\varphi}^*(x_3^{(i)}),$$
 (C35a,b)

where $\bar{\varphi}^*$ and $\bar{\Psi}^*$ are the functions (C19) and (C20) evaluated at $s=s^*$. The separation point is

$$\bar{x}_{2}^{(\text{iii})} = \bar{x}_{2}^{(\text{ii})} + \Omega\left(\frac{\pi}{2}\right), \quad \bar{x}_{3}^{(\text{iii})} = \bar{x}_{3}^{(\text{iii})} + \chi\left(\frac{\pi}{2}\right),$$
 (C36a,b)

where $\Omega(x)$ and $\chi(x)$ are the functions (C25) and (C26). The final cross-flow pair position is

$$\bar{x}_2^{(\text{iv})} = \bar{x}_2^{(\text{iii})} + \bar{\Psi}^*(x_2^{(\text{iii})}), \quad \bar{x}_3^{(\text{iv})} = \bar{x}_3^{(\text{iii})} + \bar{\varphi}^*(x_3^{(\text{iii})}).$$
 (C37*a,b*)

The above results are combined to obtain the net relative and pair displacements

$$\Delta x_k = x_k^{(iv)} - x_k^{(i)}, \quad \Delta \bar{x}_k = \bar{x}_k^{(iv)} - \bar{x}_k^{(i)}, \quad (k = 2, 3).$$
 (C38a,b)

The net displacements of each particle, ΔX_k^{12} and ΔX_k^{21} (k=2,3), are then obtained as

$$\Delta X_k^{12} = \frac{1}{2}(\Delta \bar{x}_k - \Delta x_k), \quad \Delta X_k^{21} = \frac{1}{2}(\Delta \bar{x}_k + \Delta x_k).$$
 (C39a,b)

Examples of particle displacements are shown in figures 6 and 7.

C.3.1. Collision cross-section

Combining (C34a,b) and using

$$(x_2^{(iii)})^2 + (x_3^{(iii)})^2 = (s^*)^2, \quad (x_2^{(iv)})^2 + (x_3^{(iv)})^2 = (r_c)^2,$$
 (C40*a,b*)

yields the radius of the upstream collision cross-section,

$$\frac{r_c}{\bar{a}} = \left[\left(\frac{s^*}{\varphi^*} \right)^2 - \Psi^* \right]^{1/2},\tag{C41}$$

where φ^* and Ψ^* are the mobility function integrals (C15) and (C16) evaluated on the contact surface, $s = s^*$. Figures 8 and 9 show the radius of the collision cross-section for equal size particles.

C.4. Contact friction

Contact friction between rough particles affects only their relative motion on the contact surface, described by (C22) and enters through the transverse relative mobility function, B^* . Frictionless solid contact corresponds to $B^* = B(s^*)$, where $s^* = 2 + \bar{\delta}$. Finite contact friction increases the value of B^* . The limit of tangentially locking particle contacts is obtained using the contact value of the mobility function for smooth spheres, i.e. $B^* = B(2)$. By increasing B^* , friction acts to move the polar angle between the particles from its incoming value, θ_0 , towards $\theta = \pi/2$ according to (C22). At the point of separation, $\phi = \pi/2$, we have

$$\left|\theta_1\left(\frac{\pi}{2}\right) - \frac{\pi}{2}\right| < \left|\theta_0 - \frac{\pi}{2}\right|,\tag{C42}$$

under the assumption that $\phi_0 < \pi/2$. Thus, friction acts to increase relative particle displacements in the X_2 -direction and diminish them in the X_3 -direction, according to (C33a,b).

C.4.1. Contacting permeable particles

The results in figure 5 of Reboucas & Loewenberg (2022) show that the contact value of the transverse relative mobility for permeable particles, B^* , has the upper and lower bounds,

$$B(s_{ea}^*) < B^* \le B(2),$$
 (C43)

where B(2) is the contact value of the hard-sphere mobility function, corresponding to rough particles with tangentially locking particle contacts; the equality holds for $\kappa=1$ because permeability has no effect on the transverse relative mobility for equal-size particles (Reboucas & Loewenberg 2022). The quantity $B(s_{eq}^*)$ corresponds to frictionless contact between particles with equivalent roughness, where $s_{eq}^*=2+\bar{\delta}_{eq}$ with $\bar{\delta}_{eq}$ defined by (4.1). Accordingly, particle displacements for permeable particles lie between the displacements for equivalent rough particles with frictionless and tangentially locking particle contacts.

REFERENCES

- AARTS, P.A., VAN DEN BROEK, S.A., PRINS, G.W., KUIKEN, G.D., SIXMA, J.J. & HEETHAAR, R.M. 1988 Blood platelets are concentrated near the wall and red blood cells, in the center in flowing blood. *Arteriosclerosis* 8 (6), 819–824.
- ADLER, P.M. 1981 Streamlines in and around porous particles. J. Colloid Interface Sci. 81 (2), 531-535.
- ARP, P.A. & MASON, S.G. 1977 The kinetics of flowing dispersions. J. Colloid Interface Sci. 61, 44-61.
- BANDYOPADHYAY, S., PERALTA-VIDEA, J.R. & GARDEA-TORRESDEY, J.L. 2013 Advanced analytical techniques for the measurement of nanomaterials in food and agricultural samples: a review. *Environ. Engng Sci.* 30 (3), 118–125.
- BARBATI, A.C., DESROCHES, J., ROBISSON, A. & MCKINLEY, G.H. 2016 Complex fluids and hydraulic fracturing. *Annu. Rev. Chem. Biomol. Engng* 7, 415–453.
- BATCHELOR, G.K. & GREEN, J.T. 1972a The determination of the bulk stress in a suspension of spherical particles to order c². J. Fluid Mech. **56** (2), 401–427.
- BATCHELOR, G.K. & GREEN, J.T. 1972b The hydrodynamic interaction of two small freely-moving spheres in a linear flow field. J. Fluid Mech. 56, 375–400.
- BOSSIS, G. & BRADY, J.F. 1987 Self-diffusion of brownian particles in concentrated suspensions under shear. J. Chem. Phys. 87, 5437.
- CAROTENUTO, C., REXHA, G., MARTONE, R. & MINALE, M. 2021 The microstructural change causing the failure of the cox-merz rule in newtonian suspensions: experiments and simulations. *Rheol. Acta* **60**, 309–325.
- CHANG, C. & POWELL, R.L. 1994 Self-diffusion of bimodal suspensions of hydrodynamically interacting spherical particles in shearing flow. *J. Fluid Mech.* **281**, 51–80.
- CHIEN, W., GOMPPER, G. & FEDOSOV, D.A. 2021 Effect of cytosol viscosity on the flow behavior of red blood cell suspensions in microvessels. *Microcirculation* 28 (2), e12668.
- CHUN, B., PARK, J.S., JUNG, H.W. & WON, Y.Y. 2019 Shear-induced particle migration and segregation in non-Brownian bidisperse suspensions under planar poiseuille flow. *J. Rheol.* **63** (3), 437–453.
- COLÓN QUINTANA, J.L., HECKNER, T., CHRUPALA, A., POLLOCK, J., GORIS, S. & OSSWALD, T. 2019 Experimental study of particle migration in polymer processing. *Polym. Compos.* 40 (6), 2165–2177.
- DA CUNHA, F.R. & HINCH, E.J. 1996 Shear-induced dispersion in a dilute suspension of rough spheres. J. Fluid Mech. 309, 211–223.
- Dahl, J.B., Lin, J.M.G., Muller, S.J. & Kumar, S. 2015 Microfluidic strategies for understanding the mechanics of cells and cell-mimetic systems. *Annu. Rev. Chem. Biomol. Engng* 6, 293–317.
- DENN, M.M. & MORRIS, J.F. 2014 Rheology of non-Brownian suspensions. *Annu. Rev. Chem. Biomol. Engng* 5, 203–228.
- DIEZ-SILVA, M., DAO, M., HAN, J., LIM, C.T. & SURESH, S. 2010 Shape and biomechanical characteristics of human red blood cells in health and disease. *MRS Bull.* **35** (5), 382–388.
- DUPRAT, C. & STONE, H.A. 2016 Chapter 2: low-reynolds-number flows. In *Fluid-Structure Interactions in Low-Reynolds-Number Flows*. Royal Society of Chemistry. pp. 25–77.
- ECKSTEIN, E., BAILEY, D. & SHAPIRO, A. 1977 Self-diffusion of particles in shear flow of a suspension. J. Fluid Mech. 79, 191–208.

- EILERS, H 1943 Die viskositäts-konzentrationsabhängigkeit kolloider systeme in organischen lösungsmitteln. *Kolloidn. Z.* **102** (2), 154–169.
- ELIAS, L., FENOUILLOT, F., MAJESTÉ, J.C., MARTIN, G. & CASSAGNAU, P. 2008 Migration of nanosilica particles in polymer blends. *J. Polym. Sci. B: Polym. Phys.* 46 (18), 1976–1983.
- FAHRAEAUS, R. & LINDQVIST, T. 1931 The viscosity of the blood in narrow capillary tubes. *Am. J. Physiol.* **96**, 562–568.
- Frank, M., Anderson, D., Weeks, E.R. & Morris, J.F. 2003 Particle migration in pressure-driven flow of a Brownian suspension. *J. Fluid Mech.* **493**, 363–378.
- GADALA-MARIA, F. & ACRIVOS, A. 1980 Shear-induced structure in a concentrated suspension of solid spheres. J. Rheol. 24 (6), 799–814.
- HAMPTON, R.E., MAMMOLI, A.A., GRAHAM, A.L., TETLOW, N & ALTOBELLI, S.A. 1997 Migration of particles undergoing pressure-driven flow in a circular conduit. *J. Rheol.* 41 (3), 621–640.
- HIGGINS, J.M., EDDINGTON, D.T., BHATIA, S.N. & MAHADEVAN, L. 2007 Sickle cell vasoocclusion and rescue in a microfluidic device. *Proc. Natl Acad. Sci.* **104** (51), 20496–20500.
- HUSBAND, D.M., MONDY, L.A., GANANI, E. & GRAHAM, A.L. 1994 Direct measurements of shear-induced particle migration in suspensions of bimodal spheres. *Rheol. Acta* 33 (3), 185–192.
- INGBER, M.S. & ZINCHENKO, A.Z. 2012 Semi-analytic solution of the motion of two spheres in arbitrary shear flow. *Intl J. Multiphase Flow* **42**, 152–163.
- JABBARI, M., BULATOVA, R., TOK, A.I.Y., BAHL, C.R.H., MITSOULIS, E. & HATTEL, J.H. 2016 Ceramic tape casting: a review of current methods and trends with emphasis on rheological behaviour and flow analysis. *Mater. Sci. Engng*: B 212, 39–61.
- KANEHL, P. & STARK, H. 2015 Hydrodynamic segregation in a bidisperse colloidal suspension in microchannel flow: a theoretical study. *J. Chem. Phys.* 142 (21), 214901.
- KARNIS, A, GOLDSMITH, H.L. & MASON, S.G. 1966 The kinetics of flowing dispersions: I. concentrated suspensions of rigid particles. *J. Colloid Interface Sci.* 22 (6), 531–553.
- KING, M.R. & LEIGHTON, D.T. 2001 Measurement of shear-induced dispersion in a dilute suspension. *Phys. Fluids* **13**, 397–406.
- KOCH, D.L. 1989 On hydrodynamic diffusion and drift in sheared suspensions. Phys. Fluids A 1, 1742–1745.
- KOH, C.J., HOOKHAM, P. & LEAL, L.G. 1994 An experimental investigation of concentrated suspension flows in a rectangular channel. *J. Fluid Mech.* **266**, 1–32.
- KREMER, K., ROBBINS, M.O. & GREST, G.S. 1986 Phase diagram of Yukawa systems: model for charge-stabilized colloids. Phys. Rev. Lett. 57, 2694–2697.
- KRIEGER, I.M. 1972 Rheology of monodisperse latices. Adv. Colloid Interface Sci. 3 (2), 111-136.
- KUMAR, A. & GRAHAM, M.D 2011 Segregation by membrane rigidity in flowing binary suspensions of elastic capsules. *Phys. Rev.* E **84** (6), 066316.
- KUMAR, A. & GRAHAM, M.D. 2012 Mechanism of margination in confined flows of blood and other multicomponent suspensions. *Phys. Rev. Lett.* 109 (10), 108102.
- KUMAR, A, RIVERA, R.G.H & GRAHAM, M.D. 2014 Flow-induced segregation in confined multicomponent suspensions: effects of particle size and rigidity. *J. Fluid Mech.* **738**, 423–462.
- LAC, E. & BARTHÈS-BIESEL, D. 2008 Pairwise interaction of capsules in simple shear flow: three-dimensional effects. *Phys. Fluids* **20**, 040801.
- LEIGHTON, D.T. & ACRIVOS, A. 1987a Measurement of shear-induced self-diffusion in concentrated suspensions of spheres. J. Fluid Mech. 177, 109–131.
- LEIGHTON, D.T. & ACRIVOS, A. 1987b The shear-induced migration of particles in concentrated suspensions. J. Fluid Mech. 181, 415–439.
- LENTLE, R.G. & JANSSEN, P.W.M. 2010 Manipulating digestion with foods designed to change the physical characteristics of digesta. *Crit. Rev. Food Sci. Nutrition* **50** (2), 130–145.
- LIN, C.J., LEE, K.J. & SATHER, N.F. 1970 Slow motion of two spheres in a shear field. *J. Fluid Mech.* 43, 35–47.
- LOEWENBERG, M. & HINCH, E.J. 1997 Collision of two deformable drops in shear flow. *J. Fluid Mech.* 338, 299–315.
- LOPEZ, M. & GRAHAM, M.D. 2007 Shear-induced diffusion in dilute suspensions of spherical or nonspherical particles: effects of irreversibility and symmetry breaking. *Phys. Fluids* **19**, 073602.
- LYON, M.K. & LEAL, L.G. 1998a An experimental study of the motion of concentrated suspensions in two-dimensional channel flow. Part 1. Monodisperse systems. *J. Fluid Mech.* **363**, 25–56.
- Lyon, M.K. & Leal, L.G. 1998b An experimental study of the motion of concentrated suspensions in two-dimensional channel flow. Part 2. Bidisperse systems. *J. Fluid Mech.* **363**, 57–77.
- MALIPEDDI, A.R. & SARKAR, K. 2019a Collective diffusivity in a sheared viscous emulsion: effects of viscosity ratio. *Phys. Rev. Fluids* **4** (9), 093603.

- MALIPEDDI, A.R. & SARKAR, K. 2019b Shear-induced collective diffusivity down a concentration gradient in a viscous emulsion of drops. *J. Fluid Mech.* **868**, 5–25.
- MIGLER, K.B. 2001 String formation in sheared polymer blends: coalescence, breakup, and finite size effects. *Phys. Rev. Lett.* **86**, 1023–1026.
- MORRIS, J.F. 2009 A review of microstructure in concentrated suspensions and its implications for rheology and bulk flow. *Rheol. Acta* 48 (8), 909–923.
- MORRIS, J.F. & BRADY, J.F. 1998 Pressure-driven flow of a suspension: buoyancy effects. *Intl J. Multiphase Flow* **24**, 105–130.
- NARSIMHAN, V., ZHAO, H. & SHAQFEH, E.S.G. 2013 Coarse-grained theory to predict the concentration distribution of red blood cells in wall-bounded Couette flow at zero Reynolds number. *Phys. Fluids* 25, 061901
- NEMER, M.B., CHEN, X., PAPADOPOULOS, D.H., BLAWZDZIEWICZ, J. & LOEWENBERG, M. 2004 Hindered and enhanced coalescence of drops in stokes flows. *Phys. Rev. Lett.* **92**, art. 114501.
- NEMER, M.B., CHEN, X., PAPADOPOULOS, D.H., BŁAWZDZIEWICZ, J. & LOEWENBERG, M. 2007 Comment on "Two touching spherical drops in uniaxial extensional flow: analytic solution to the creeping flow problem". *J. Colloid Interface Sci.* 308 (1), 1–3.
- NEMER, M.B., SANTORO, P., CHEN, X., BLAWZDZIEWICZ, J. & LOEWENBERG, M. 2013 Coalescence of drops with mobile interfaces in a quiescent fluid. *J. Fluid Mech.* 728, 471–500.
- NOTT, P.R. & BRADY, J.F. 1994 Pressure-driven flow of suspensions: simulation and theory. *J. Fluid Mech.* **275**, 157–199.
- NOTT, P.R., GUAZZELLI, E. & POULIQUEN, O. 2011 The suspension balance model revisited. *Phys. Fluids* **23** (4), 043304.
- OMORI, T., ISHIKAWA, T., IMAI, Y. & YAMAGUCHI, T. 2013 Shear-induced diffusion of red blood cells in a semi-dilute suspension. J. Fluid Mech. 724, 154–174.
- OSIPTSOV, A.A. 2017 Fluid mechanics of hydraulic fracturing: a review. J. Petrol. Sci. Engng 156, 513–535.
- PHAN-THIEN, N & FANG, Z 1996 Entrance length and pulsatile flows of a model concentrated suspension. J. Rheol. 40 (4), 521–548.
- PHILLIPS, R.J., ARMSTRONG, R.C., BROWN, R.A., GRAHAM, A.L. & ABBOTT, J.R. 1992 A constitutive equation for concentrated suspensions that accounts for shear-induced particle migration. *Phys. Fluids A: Fluid Dyn.* 4, 30–40.
- PRANAY, P., ANEKAL, S.G, HERNANDEZ-ORTIZ, J.P & GRAHAM, M.D 2010 Pair collisions of fluid-filled elastic capsules in shear flow: effects of membrane properties and polymer additives. *Phys. Fluids* **22** (12), 123103.
- PRIES, A.R., NEUHAUS, D. & GAEHTGENS, P. 1992 Blood viscosity in tube flow: dependence on diameter and hematocrit. *Am. J. Physiol. Heart Circ. Physiol.* **263** (6), H1770–H1778.
- QI, Q.M. & SHAQFEH, E.S.G. 2017 Theory to predict particle migration and margination in the pressure-driven channel flow of blood. *Phys. Rev. Fluids* 2 (9), 093102.
- QI, Q.M. & SHAQFEH, E.S.G. 2018 Time-dependent particle migration and margination in the pressure-driven channel flow of blood. *Phys. Rev. Fluids* **3** (3), 034302.
- RAMACHANDRAN, A., LOEWENBERG, M. & LEIGHTON, D.T. 2010 A constitutive equation for droplet distribution in unidirectional flows for low capillary numbers. *Phys. Fluids* 22, 083301.
- RAMPALL, I., SMART, J.R. & LEIGHTON, D.T. 1997 The influence of surface roughness on the particle-pair distribution function of dilute suspensions of non-colloidal spheres in simple shear flow. *J. Fluid Mech.* 339, 1–24.
- REBOUCAS, R.B. & LOEWENBERG, M. 2021a Near-contact approach of two permeable spheres. J. Fluid Mech. 925, A1.
- REBOUCAS, R.B. & LOEWENBERG, M. 2021b Collision rates of permeable particles in creeping flows. *Phys. Fluids* **33**, 083322.
- REBOUCAS, R.B & LOEWENBERG, M. 2022 Resistance and mobility functions for the near-contact motion of permeable particles. *J. Fluid Mech.* **938**, A27.
- REBOUCAS, R.B., SIQUEIRA, I.R., MENDES, P.R.D. & CARVALHO, M.S. 2016 On the pressure-driven flow of suspensions: particle migration in shear sensitive liquids. *J. Non-Newtonian Fluid Mech.* **234**, 178–187.
- REDDIG, S. & STARK, H. 2013 Nonlinear dynamics of spherical particles in poiseuille flow under creeping-flow condition. *The J. Chem. Phys.* **138** (23), 234902.
- REDDY, M.M. & SINGH, A. 2019 Shear-induced particle migration and size segregation in bidisperse suspension flowing through symmetric t-shaped channel. *Phys. Fluids* **31** (5), 053305.
- RIVERA, R.G.H., SINHA, K. & GRAHAM, M.D 2015 Margination regimes and drainage transition in confined multicomponent suspensions. *Phys. Rev. Lett.* 114 (18), 188101.

- RIVERA, R.G.H., ZHANG, X. & GRAHAM, M.D. 2016 Mechanistic theory of margination and flow-induced segregation in confined multicomponent suspensions: simple shear and poiseuille flows. *Phys. Rev. Fluids* 1, 060501.
- ROTHER, M.A. & DAVIS, R.H. 2001 The effect of slight deformation on droplet coalescence in linear flows. *Phys. Fluids* **13** (5), 1178–1190.
- SANTORO, P. & LOEWENBERG, M. 2009 Coalescence of drops with tangentially mobile interfaces: effects of ambient flow. *Ann. N.Y. Acad. Sci.* **1161** (1), 277–291.
- SARKAR, K. & SINGH, R.K. 2013 Spatial ordering due to hydrodynamic interactions between a pair of colliding drops in a confined shear. *Phys. Fluids* 25, 051702.
- SCHROEN, K., VAN DINTHER, A. & STOCKMANN, R. 2017 Particle migration in laminar shear fields: a new basis for large scale separation technology? *Separation Purification Technol.* **174**, 372–388.
- SCHROËN, K., DE RUITER, J. & BERTON-CARABIN, C.C. 2020 Microtechnological tools to achieve sustainable food processes, products, and ingredients. *Food Engng Rev.* 12, 101–120.
- SECOMB, T.W. 2017 Blood flow in the microcirculation. Annu. Rev. Fluid Mech. 49, 443–461.
- SECOMB, T.W. & PRIES, A.R. 2013 Blood viscosity in microvessels: experiment and theory. C. R. Phys. 14 (6), 470–478.
- SEMWOGERERE, D., MORRIS, J.F. & WEEKS, E.R. 2007 Development of particle migration in pressure-driven flow of a brownian suspension. *J. Fluid Mech.* **581**, 437–451.
- SEMWOGERERE, D. & WEEKS, E.R. 2008 Shear-induced particle migration in binary colloidal suspensions. *Phys. Fluids* **20**, 043306.
- SHAULY, A., WACHS, A. & NIR, A. 1998 Shear-induced particle migration in a polydisperse concentrated suspension. *J. Rheol.* 42 (6), 1329–1348.
- SINGH, R.K. & SARKAR, K. 2015 Hydrodynamic interactions between pairs of capsules and drops in a simple shear: effects of viscosity ratio and heterogeneous collision. *Phys. Rev.* E **92**, 063029.
- SINGHA, S., MALIPEDDI, A.R., ZURITA-GOTOR, M., SARKAR, K., SHEN, K., LOEWENBERG, M., MIGLER, K.B. & BLAWZDZIEWICZ, J. 2019 Mechanisms of spontaneous chain formation and subsequent microstructural evolution in shear-driven strongly confined drop monolayers. *Soft Matt.* 15 (24), 4873–4889.
- VAN DER SMAN, R.G.M. 2009 Simulations of confined suspension flow at multiple length scales. Soft Matt. 5 (22), 4376–4387.
- SMART, J.R., BEIMFOHR, S. & LEIGHTON, D.T. 1993 Measurement of the translational and rotational velocities of a noncolloidal sphere rolling down a smooth inclined place at low reynolds number. *Phys. Fluids* A 5, 13–24.
- SMART, J.R. & LEIGHTON, D.T. 1989 Measurement of the hydrodynamic surface roughness of noncolloidal spheres. *Phys. Fluids* A: *Fluid Dyn.* 1 (1), 52–60.
- STICKEL, J.J. & POWELL, R.L. 2005 Fluid mechanics and rheology of dense suspensions. Annu. Rev. Fluid Mech. 37, 129–149.
- TANGELDER, G.J., TEIRLINCK, H.C., SLAAF, D.W. & RENEMAN, R.S. 1985 Distribution of blood platelets flowing in arterioles. *Am. J. Physiol. Heart Circ. Physiol.* 248 (3), H318–H323.
- TANNER, R.I. 2018 Aspects of non-colloidal suspension rheology. *Phys. Fluids* **30** (10), 101301.
- TOKAREV, A., PANASENKO, G. & ATAULLAKHANOV, F. 2011 Segregation of flowing blood: mathematical description. *Math. Model. Natural Phenomena* 6 (5), 281–319.
- VAN DINTHER, A.M.C., SCHROËN, C.G.P.H., VERGELDT, F.J., VAN DER SMAN, R.G.M. & BOOM, R.M. 2012 Suspension flow in microfluidic devices—a review of experimental techniques focussing on concentration and velocity gradients. Adv. Colloid Interface Sci. 173, 23–34.
- WANG, H., ZINCHENKO, A.Z. & DAVIS, R.H. 1994 The collision rate of small drops in linear flow fields. *J. Fluid Mech.* 265, 161–188.
- WILSON, H.J. 2005 An analytic form for the pair distribution function and rheology of a dilute suspension of rough spheres in plane strain flow. *J. Fluid Mech.* **534**, 97–114.
- ZARRAGA, I.E. & LEIGHTON, D.T. 2001 Shear-induced diffusivity on a dilute bidisperse suspension of hard spheres. *J. Colloid Interface Sci.* 243, 503–514.
- ZHAO, H. & SHAQFEH, E.S.G. 2011 Shear-induced platelet margination in a microchannel. *Phys. Rev.* E 83, 061924.
- ZHAO, H., SHAQFEH, E.S.G. & NARSIMHAN, V. 2012 Shear-induced particle migration and margination in a cellular suspension. *Phys. Fluids* **24** (1), 011902.
- ZINCHENKO, A.Z. 1978 Calculation of hydrodynamic interaction between drops at low reynolds numbers. Z. Angew. Math. Mech. 42 (5), 1046–1051.
- ZINCHENKO, A.Z. 1980 The slow asymmetric motion of two drops in a viscous medium. Z. Angew. Math. Mech. 44 (1), 30–37.

- ZINCHENKO, A.Z. 1983 Hydrodynamic interaction of two identical liquid spheres in linear flow field. Z. Angew. Math. Mech. 47 (1), 37–43.
- ZINCHENKO, A.Z. 1984 Effect of hydrodynamic interactions between the particles on the rheological properties of dilute emulsions. Z. Angew. Math. Mech. 48 (2), 198–206.
- ZINCHENKO, A.Z. & DAVIS, R.H. 2005 A multipole-accelerated algorithm for close interaction of slightly deformable drops. *J. Comput. Phys.* **207** (2), 695–735.
- ZURITA-GOTOR, M., BŁAWZDZIEWICZ, J. & WAJNRYB, E. 2012 Layering instability in a confined suspension flow. *Phys. Rev. Lett.* **108** (6), 068301.